analytical chemistry

Review

pubs.acs.org/ac

Spectroscopic Imaging at the Nanoscale: Technologies and Recent Applications

Lifu Xiao and Zachary D. Schultz*

Department of Chemistry and Biochemistry, University of Notre Dame, Notre Dame, Indiana 46556, United States

CONTENTS

Advances in technology now enable infrared and Raman vibrational spectroscopic imaging with resolution on the molecular scale. A number of techniques have emerged that provide spectroscopic imaging with nanometer scale resolution including tip-enhanced Raman scattering (TERS), infrared scattering-type scanning near-field optical microscopy (IR s-SNOM), atomic force microscopy infrared (AFM-IR), and photo-induced force microscopy (PiFM). In this review, we profile recent advances in nanoscale spectroscopic imaging, discussing differences in the methods, highlighting recent technical advances, and reporting applications with each approach.

Since the first demonstrations showing that spectroscopy can inform about the chemical composition of images in a microscope,[1] researchers have investigated advances in instrumentation to improve the sensitivity, spatial resolution, and specificity of these spectroscopic imaging techniques.[2−5] In particular, the chemical rich signals of vibrational spectroscopies, both infrared and Raman, have attracted considerable interest. Applications of infrared and Raman spectroscopic imaging span diverse applications from biomedical diagnostics to forensics, cultural heritage, and materials characterization.[6−9]

There have been a number of recent advances using vibrational signals as markers for selective imaging.[10] For example, a recent study showed the vibrational signal of a triple bond made an effective tag for more sensitive stimulated Raman imaging.[11] Other examples include the development of surface enhanced Raman tags, where a specific enhanced signal marks an analyte of interest.[12,13] We limit our review to reports that measure a spectrum to discriminate and identify molecular components, or changes in molecular components, using the detected spectroscopic signals.

Improvements in hardware have been particularly influential in advancing infrared and Raman imaging. In particular, the past few years have seen the commercialization of a number of techniques, which combine vibrational spectroscopy with scanning probe microscopes to provide spectroscopic imaging on nanometer length scales. These techniques, including TERS, IR s-SNOM, AFM-IR, and PiFM, are providing unprecedented spatial resolution and chemical contrast. In many ways these techniques appear quite similar and the differences between the techniques can be difficult to discern. In all of these methodologies, an optical response (e.g., absorption, scattering, induced dipole) is combined with a scanning probe microscope to provide increased spatial resolution and increased sensitivity. Many of these techniques are enabled by advances in instrumentation and suggest increased facility obtaining experimental results by nonexperts.

TERS

TERS combines Raman spectroscopy and scanning probe microscopy to provide an ultrasensitive approach for spectroscopic imaging at the nanoscale, beyond the diffraction limit. TERS uses a nanostructured metallic scanning probe microscope tip to confine and enhance the electric field of the incident light at the tip apex and therefore generate enhanced Raman scattering from molecules within immediate proximity of the tip. By scanning a sample under the TERS tip, a Raman image with chemical specific information can be obtained with spatial resolution on the scale of the confined near-field. Since the first introduction of TERS in 2000,[14−17] significant progress has been made in the understanding of TERS mechanisms, development of TERS techniques, and the application of TERS

Special Issue: Fundamental and Applied Reviews in Analytical Chemistry 2018

Published: October 13, 2017

DOI: 10.1021/acs.analchem.7b04151
Anal. Chem. 2018, 90, 440−458

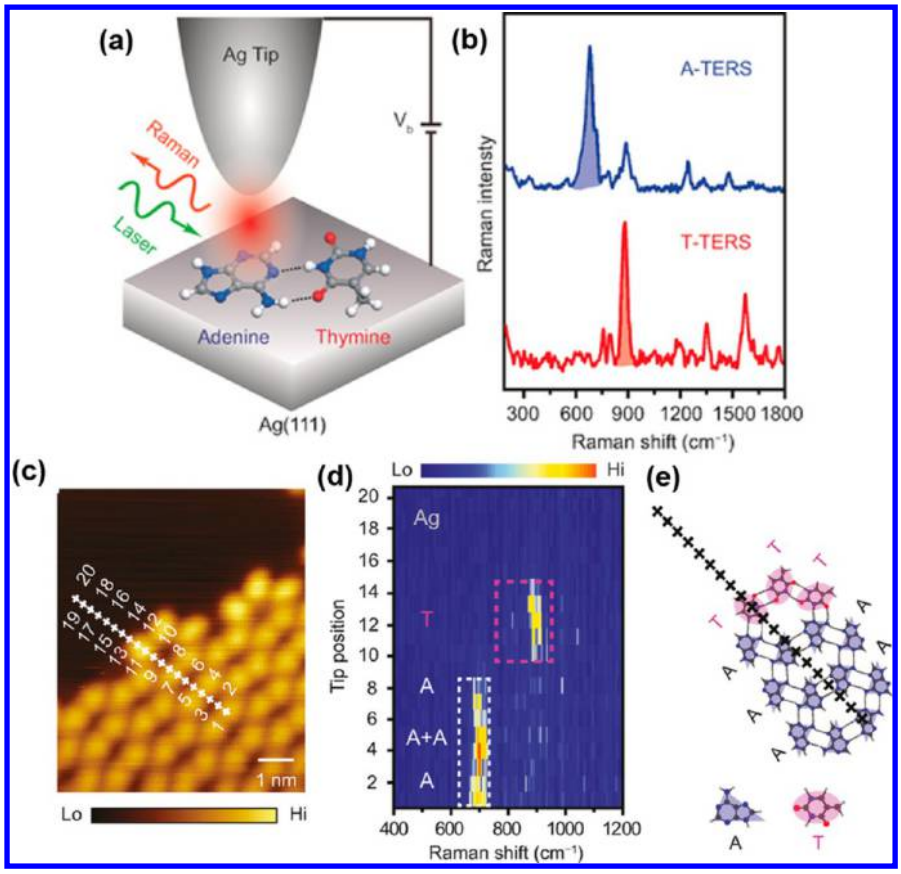

Figure 1. (a) Schematic of STM-controlled TERS in a confocal-type side-illumination configuration on Ag(111) using Ag tips. (b) Representative TERS spectra of adenine (A, blue) and thymine (T, red). Each spectrum is normalized to the strongest peak (680 cm^{-1} in the TERS spectrum of A and 881 cm^{-1} in that of T) and then shifted vertically for clarity. (c) High-resolution STM imaging around the coadsorption boundary. (d) Corresponding spectral evolution for 20 sequential TERS measurements along the line trace marked by crosses in part c with a step size of 0.27 nm. (e) A proposed molecular arrangement along the line trace in part c. Reproduced from Distinguishing Individual DNA Bases in a Network by Non-Resonant Tip-Enhanced Raman Scattering, Zhang, R.; Zhang, X.; Wang, H.; Zhang, Y.; Jiang, S.; Hu, C.; Zhang, Y.; Luo, Y.; Dong, Z. *Angew. Chem. Int. Ed. Engl.*, Vol. 56, Issue 20 (ref 46). Copyright 2017 Wiley.

to various problems. Thorough reviews of the theory, technical details, and experimental setups of TERS can be found elsewhere.[18−22] Here we review the most recent advances in TERS and its applications as a spectroscopic imaging technique.

Technical Advances of TERS. *TERS Tip Fabrication.* A plasmonic metal tip is the most critical component in TERS that serves as a near-field optical antenna, which confines the propagating far-field radiation to the strongly localized electromagnetic near field. Since the size, shape, and composition of the TERS tip strongly affect the localized surface plasmon resonance, which further affects the detected TERS signal, it is important to develop fabrication procedures that can produce tips with high enhancement factors and reproducible geometries.

A common way to fabricate solid metal (e.g., Ag and Au) tips, typically used in STM-TERS, is electrochemical etching, which electrochemically dissolves a metal wire in the etching electrolyte.[23−27] By adjusting the etching parameters, the size and shape of the etched tip can be controlled.[24] Recent studies have also shown that the etchant composition and concentration affect the shape of the resulting tips.[26,27] However, it is still difficult to precisely tune the tip size and shape by electrochemical etching alone. Overetching is a common problem, particularly in the case of silver tips. To address this problem, the Ren group developed an optical method that uses a machine vision system to monitor the fabrication process of silver tips and quickly cut off the etching circuit once the tip forms.[23]

In the case of AFM-TERS, metal-coated tips are often used. These tips are fabricated by the deposition or attachment of Au or Ag onto commercially available AFM tips. Compared to electrochemically etched metal tips, metal-coated TERS tips typically have better-defined geometry and thus generate more reproducible TERS signals.

Other approaches to fabricating metal-coated TERS tips are to attach presynthesized plasmonic nanostructures to the end of an AFM tip. Leiterer et al. successfully demonstrated TERS from a tip prepared by positioning individual presynthesized plasmonic nanoparticles on commercial AFM tips by dielectrophoresis.[28] Kim et al. used a DNA linker to attach Au nanoparticles onto AFM tips and then used the attached Au as a core to facilitate the deposition of an Ag shell.[29] In a recent study, AFM tips were coated with self-assembled monolayers of block copolymers loaded with clusters of bimetallic, gold and silver nanoparticle heterostructures to form highly enhancing TERS tips.[30] By varying the nanometal loadings into the polymer micelles, the resulting tip properties were optimized for reproducibility.

The direct deposition of metals onto the apex of conductive AFM tips can also produce TERS tips. Applying short potential pulses between the tip and a sacrificial electrode in close proximity electrochemically deposits noble metals onto

DOI: 10.1021/acs.analchem.7b04151
Anal. Chem. 2018, 90, 440−458

commercial AFM tips.[31−33] The morphology and radius of the coated tips are controlled by the deposition potential and deposition time with high reproducibility, which enabled a systematic investigation of the effect of tip radius on the TERS enhancement. Ma et al. reported a method for the local deposition of spherical Au or Ag onto optically inactive W- or C-tips, which is achieved by the local charging of the electrodes with short pulses and the local buildup of the ion concentration.[32] By tuning the pulse duration, deposition time, and gap distance between the tip and the electrode, the diameter of the deposited nanospheres was varied from tens of nanometers to one micrometer. Bakhti and co-workers reported a technique to grow single gold filaments based on a bias-assisted electro-reduction of gold ions directly at the AFM tip apex.[33] The length of the formed filaments can be tuned from tens to hundreds of nanometers and the radius can be as low as a few nanometers, though the TERS performance remains to be evaluated.

Recently, Taguchi et al. reported using standard vacuum vapor deposition to fabricate multiple metal grains on SiO_2 AFM tips, in order to produce high and reproducible enhancement in TERS.[34] Their experiments and simulations showed that the plasmonic enhancement strongly depends on the number of grains and the grain separation. Multiple grains arranged closely but discretely (within a few nanometers) on a dielectric probe act as an efficient plasmonic antenna. One challenge of the standard vacuum vapor deposition method is to accurately control the size and shape of the evaporated tips. A novel way to overcome this challenge is to use focused ion beam (FIB) milling to provide a precise control of the shape of the tips. Several groups have reported FIB milling based methods to precisely control the fabrication of plasmonic metal tips with tunable length and shape.[35,36] These studies demonstrated that by varying the geometry of the tips, the localized surface plasmon resonance (LSPR) can be fine-tuned at a desired absorption channel that favors the TERS experiments. It is worth noting that the LSPR scattering spectra from the tip apex depends on the polarization of the incident light; therefore, optimization of TERS measurements can be achieved by tuning the excitation polarization to induce the largest LSPR signal.[37]

A common issue with TERS tips is the short lifetime. The typical Au or Ag tips are prone to unwanted chemisorption in air, which may interfere with the detected TERS signal. In addition, atmospheric corrosion of Ag tips greatly compromises their use in TERS experiments within just a few days. Several studies have been carried out to improve the chemical stability and extend the plasmonic lifetime of the tips.[38−40] The Zenobi group developed a simple electrochemical method for recovering the corroded Ag tips and showed that the recovered tips have a field enhancement factor comparable to freshly prepared Ag tips.[38] Another way to prevent atmospheric corrosion of Ag tips is to isolate oxygen from the storage environment of the tips. The Roy group systematically investigated the plasmonic degradation of Ag tip under different environmental conditions and demonstrated that the low oxygen and low moisture environment in a glovebox can significantly extend the lifetime of Ag tips from a few hours to several months.[39] In another study, the Zenobi group demonstrated that by coating an ultrathin and pinhole-free silica shell on top of the noble-metal nanostructures, the strongly enhancing tips are protected from undesired chemisorption and have a significantly longer lifetime than unprotected tips.[40]

Subnanometer Spatial Resolution. High spatial resolution is one of the intrinsic features of TERS. Recently, multiple studies have achieved spatial resolution of 1 nm and lower.[41−46] Using STM-TERS under ultrahigh-vacuum (UHV) and low temperature conditions, the Dong group successfully distinguished adjacent molecules of similar chemical structures with a spatial resolution of ∼0.6 nm.[42] The same research group also reported TERS imaging of individual DNA bases with similar subnanometer resolution (Figure 1).[46] The characteristic TERS peaks were chosen as the spectral fingerprint for rapid differentiation, demonstrating the potential of TERS as a new method to realize single-molecule DNA sequencing on surfaces. Using UHV-TERS, the Van Duyne group interrogated the conformational switch between two metastable surface-mediated isomers on Cu(111) at room temperature, demonstrating the ability to unambiguously distinguish the conformational differences between neighboring molecules with angstrom-scale spatial resolution.[44] For more applications of UHV-TERS, the Van Duyne group recently published a review in this area.[47] In addition to STM-TERS, the Deckert group reported AFM-TERS studies on protein fibrils, which reveal a surprising capability to distinguish amino acid distributions locally on a length scale of at least 1 nm.[41,45] Though recent experiments demonstrate that subnanometer spatial resolution can be achieved by TERS, the origin of this ultrahigh resolution defies the classic electromagnetic enhancement explanation and currently remains unresolved.

Several theoretical studies have been carried out in an effort to explain the origin of the super high spatial resolution observed in recent TERS experiments. Meng et al. proposed a physical mechanism suggesting the ultrahigh spatial resolution of TERS arises from the electric field gradient effect due to the tighter spatial confinement and sensitivity to the infrared-active molecules.[48] Zhang et al. proposed another theory that accounts for the strong near-field self-interaction of the molecule within the plasmonic nanogap, which strongly modulates the Raman response in both the signal intensity and spatial sensitivity.[49,50] A finite element method calculation was presented by the Deckert group, in which an atomic protrusion, or defect, on the TERS probe could account for the ultrahigh spatial resolution.[51] The same group also investigated the influence of tip-molecule conformation on the obtained Raman signal and concluded that the geometric structure of the molecule with respect to the tip could also contribute to the subnanometer spatial resolution.[52] Most recently, the Jensen group presented a systematic theoretical study of TERS imaging of single molecules, using a hybrid atomistic electrodynamics−quantum mechanical method.[53] Their work suggests that achieving the atomic resolution requires the near field to be confined within a few angstroms in diameter and the near-field focal plane to coincide with the plane of the molecule.

Applications of TERS. *TERS in Material Sciences. Carbon Materials.* TERS is most widely applied to characterize various carbon materials, such as graphene and carbon nanotubes (CNTs). These materials present simple and intense Raman bands: G-band (∼1580 cm^{-1}) attributed to in-plane vibrational modes, the 2D-band (also called G'-band, ∼2690 cm^{-1}), a second-order overtone of a different in-plane vibration, and disorder-induced D-band (∼1350 cm^{-1}). Intensities and ratios of certain bands provide information on purity, defects, edges,

DOI: 10.1021/acs.analchem.7b04151
Anal. Chem. 2018, 90, 440−458

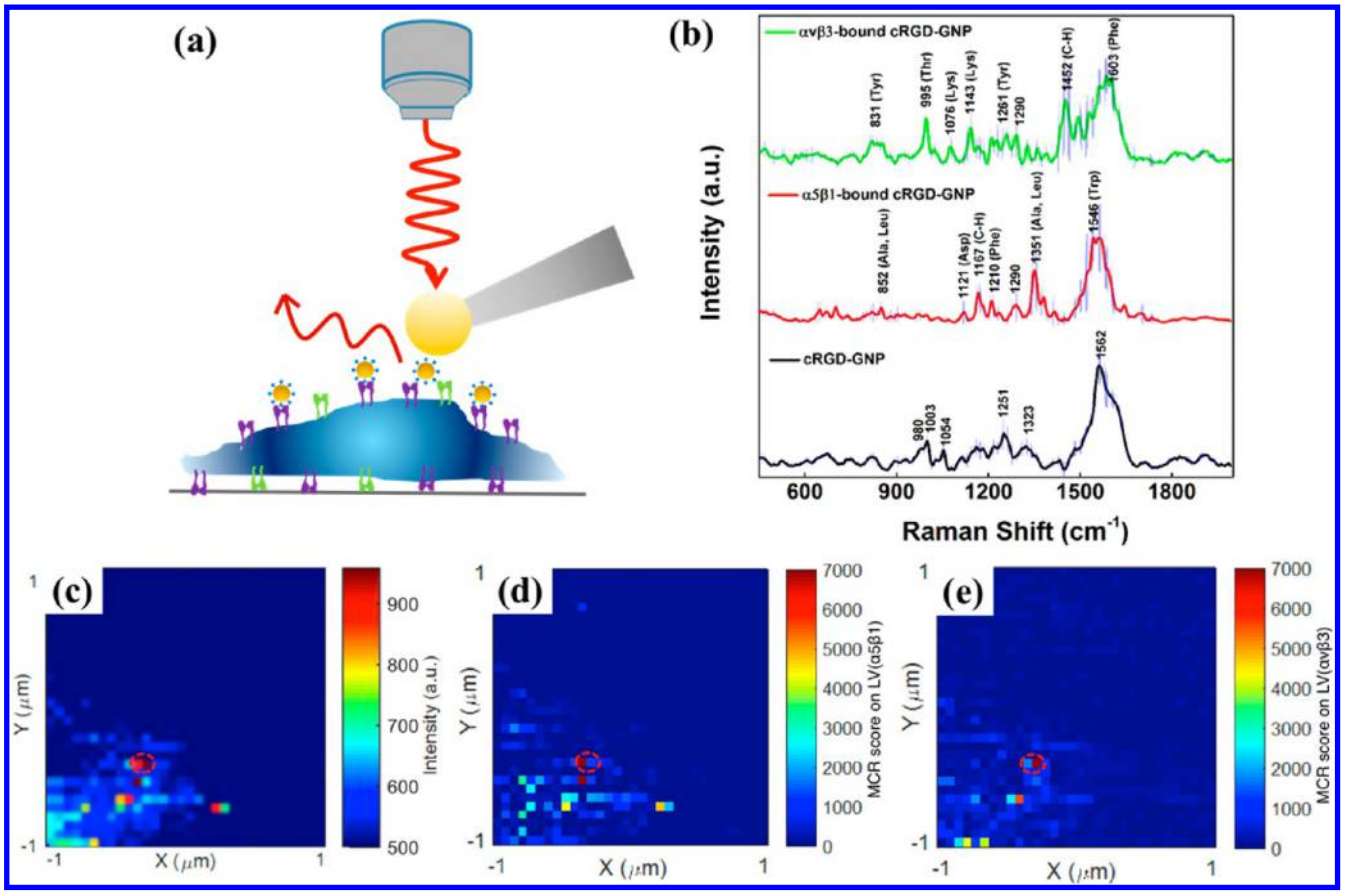

Figure 2. (a) Schematic illustration of TERS detection of integrin receptors in cell membrane. (b) Average SERS spectra of cRGD-GNPs, $\alpha5\beta1$-bound cRGD-GNPs, and $\alpha v\beta3$-bound cRGD-GNPs. Shaded area represents standard deviation. (c) TERS map of SW480 cells incubated with cRGD-GNPs, constructed with single-peak intensity at 1003 cm^{-1}. Pixel step: 62.5 nm. (d, e) MCR score maps reflecting the localization of (d) $\alpha5\beta1$ and (e) $\alpha v\beta3$ on the same cell membrane area as part c. Reproduced from Xiao, L.; Wang, H.; Schultz, Z. D. *Anal. Chem.* **2016**, *88*, 6547−6553 (ref 89). Copyright 2016 American Chemical Society.

and number of layers of these carbon materials.[54] Compared with conventional Raman spectroscopy, TERS provides detailed information about subtle structural variation of graphene and CNTs with high spatial resolution commensurate with the sizes of the materials.

Beams et al. demonstrated that a single 5 nm particle can induce a radial strain over a lateral distance of ∼170 nm in graphene by monitoring the 2D-band using TERS.[55] In another study, TERS revealed the nanoscale strain variation by ridge nanostructures, which cannot be seen with micro-Raman imaging, in SiC-grown epitaxial graphene microislands.[56] Takuya et al. investigated local doping concentration modulation of graphene flakes.[57] By spectral line scanning across the edge of graphene, the localization of the D-band enhancement was observed at the edge boundary. With a gap-mode TERS configuration, Lagugne-Labarthet and co-workers utilized distinct excitation polarizations to discriminate the edges of a graphene flake of a few layers.[58] The intensity ratio of the D/G bands provides information about the edge type and orientation of the flakes. More recently, Su et al. used nongap mode TERS to successfully map the intrinsic defects in single layer graphene with 20 nm spatial resolution.[59]

A CNT is effectively a sheet of graphene rolled in to a cylinder, with unique electrical and mechanical properties. The spectral modes of CNTs are similar to those of graphene. In a recent TERS study, the intensity ratio of 2D/G bands was found to be sensitive to the number of walls of a multiwalled CNT.[60] Moreover, TERS mapping has been demonstrated to successfully identify and characterize single-walled CNTs even fully embedded in a polymer matrix.[61] Sheremet et al. reported the nanoscale imaging and discrimination of individual constituents in a four-component carbonaceous sample using TERS, demonstrating its great potential to study complex carbon systems with high spatial resolution.[62]

Other Materials. TERS imaging has provided valuable information about the self-assembled monolayers (SAMs) of organic molecules immobilized on flat gold substrates.[63−65] The Ren group applied TERS to probe the subtle change of intermolecular interactions during the assembly of a pyridine-terminated aromatic thiol.[63] It was observed that the aromatic C═C bond stretching vibration is very sensitive to the intermolecular $\pi-\pi$ stacking and can be used to monitor the strength of the intermolecular interactions in SAMs. By using combined TERS measurements and density functional theory calculations, Zenobi and co-workers provided insight into the molecular orientation and intermolecular $\pi-\pi$ stacking interaction on monolayers prepared by different methods.[65]

Layered two-dimensional transition metal dichalcogenides (e.g., WSe_2, WS_2, MoS_2) have emerged as potential platforms for novel electronic and optical devices with properties that strongly depend on nanoscale structural heterogeneity. There are several TERS investigations into the excitonic properties of these materials.[27,66−68]

DOI: 10.1021/acs.analchem.7b04151
Anal. Chem. 2018, 90, 440−458

In addition to the above-mentioned materials, the advantages of TERS have also been exploited to study properties of other inorganic oxide samples, including iron oxide nanoparticles,[69] double perovskite thin films,[70] and strained silicon for semiconductor devices.[71]

TERS in Life Sciences. DNAs. Some interesting studies on DNA molecules have been reported lately. It was recently demonstrated that TERS is able to unambiguously distinguish two individual complementary DNA bases (adenine and thymine) with a spatial resolution down to 0.9 nm.[46] Furthermore, another study illustrated the sensitivity of TERS to detect base-to-base transitions (adenine to cytosine) in a single-strand DNA under ambient conditions.[72] TERS has also been applied to assess the chemical differences between plasmid-free DNA and plasmid-embedded DNA.[73]

In order to obtain reliable TERS signal to differentiate single bases, it is crucial to maintain a well-defined conformation of DNA molecules on the substrate, as changes in conformation or orientation of DNA gives rise to different TERS signals. Immobilization methods based on Mg/Mn ions and silanes have been reported to preserve different conformations of DNA molecules, and TERS has been successfully applied to assess the conformational changes of single DNA molecules.[74,75]

Proteins and Peptides. TERS has been applied in a number of studies on protein fibrils, including insulin fibrils,[45,76,77] prion protein amyloid fibrils,[78] milk protein β-lactoglobulin,[79] human islet amyloid precursor peptide fibrils,[80] and other disease-related peptide fibrils.[81] The high chemical sensitivity and spatial resolution of TERS enabled specific characterization of protein secondary structures and conformational changes on the fibril surface. For example, the Deckert group performed a systematic investigation of individual insulin amyloid fibrils, focusing on the identification of the secondary structure via the amide III band and the differentiation of hydrophobic and hydrophilic domains on the surface.[45] They also investigated the conformational differences of the fibrilized insulin in the presence of different inhibition agents.[76] Recently, Bonhommeau et al. demonstrated that Aβ_{1-42} peptide fibrils implicated in Alzheimer's disease can be distinguished from synthetic oligomers by measuring amide I and amide III bands using TERS.[81] It should be noted that the amide I band remains controversial in TERS experiments, as it is not always observed.[82]

Another protein-related application of TERS is to characterize the glycosylation status of individual glycoproteins and their secondary structures.[83,84] For example, TERS was successfully applied, in combination with carefully designed multivariate data analysis methods, to quantify the proportion of glycosylated protein in mixtures of native and glycosylated forms of bovine pancreatic ribonuclease.[84]

In the past few years, the Schultz group has performed a series of systematic studies to characterize the specificity of protein–ligand interactions.[85−90] In these studies, the TERS signal from the binding site of a protein can be selectively obtained by controlling the plasmonic interactions between the TERS tip and ligand-functionalized nanoparticles. Recently, the plasmonic coupling between a gold nanotip and RGD peptide-functionalized nanoparticles, which bind to specific integrin receptors, were exploited to produce enhanced Raman signals that differentiated between structurally similar integrin subtypes (i.e., $\alpha5\beta1$ and $\alpha v\beta3$) in intact cancer cell membranes (Figure 2).[89] In addition, since the measured TERS signal is highly dependent on the ligand–receptor binding conformation, perspectives about binding specificities can be obtained by analyzing the variance in TERS spectra for different ligands binding with the same receptor.[90]

Cells. TERS is a very useful tool for nanoscale chemical analysis on the surfaces of viruses, bacteria, and cells. Popp and co-workers demonstrated TERS in combination with chemometric methods to discriminate a pair of pathogenic viruses. On the basis of the compositional differences in protein and lipid components, the viruses were classified with an accuracy of 91%.[91] Hermelink et al. reported a successful strategy to analyze the morphology and chemical composition of single virus particles by correlated transmission electron microscopy and TERS.[92] Rusciano et al. achieved nanoscale chemical imaging of a single bacterial spore, localizing proteins and carbohydrates on the surface through principal component analysis of the TERS spectra.[93] Most recently, TERS was successfully used for nanoscale chemical mapping of newly synthesized phospholipid molecules from sections of mammalian cells.[94] Topically applied liposomal phospholipid migration into human stratum corneum was also tracked with TERS.[95]

Though the application of TERS in life sciences has seen a rapid increase in recent years, additional improvements are needed to fully realize its potential. It remains challenging to obtain TERS in liquid environments, although this is an area that is progressing (see below). Another necessary improvement is to further increase the sensitivity and therefore improve the imaging speed in order to monitor dynamic biological processes.

TERS in Liquids. The application of TERS in a liquid environment is challenging due to limitations like tip contamination and degradation, laser focusing, and scanning probe microscope feedback. However, the use of TERS in liquid is still of great interest as it enables the investigation of biological samples in their native states. Recently, several research groups have reported TERS measurements in liquids.[96−102] Unlike the usual strategy that applies a layer of coating to prolong the stability of the tip,[96,97] an interesting approach was reported in a recent AFM-TERS study in which probe molecules were conjugated on the TERS tip to map the local pH in an aqueous solution.[98] Other solution properties could be investigated using this approach just by modifying the TERS tip with different probe molecules.

STM-TERS also has been implemented in liquids. In 2015, the Ren group reported the first electrochemical TERS (EC-TERS) results by integrating a commercial STM system with a home-built confocal Raman microscope using a horizontal illumination approach.[99] Within weeks, the Van Duyne group reported AFM based EC-TERS to probe redox reactions of Nile Blue molecules.[100] A recent study demonstrated the feasibility of TERS in a top illumination/collection configuration for imaging of opaque samples covered by a thin layer of organic solvent.[101] Sabanes et al. presented a side-illumination STM-TERS setup to measure a monolayer of thiophenol on gold in water.[102]

Though there is an increasing number of publications applying TERS in liquids using different illumination configurations (e.g., top-, bottom-, side-illuminations), it remains experimentally challenging for imaging.

Other Applications. A novel application of TERS is to map the catalytic activities of surfaces and nanostructures with nanoscale spatial resolution. The Roy group demonstrated the chemical imaging of photocatalytic oxidation of *p*-mercaptoaniline to *p*,*p*′-dimercaptoazobenzene (DMAB) using AFM-

DOI: 10.1021/acs.analchem.7b04151
Anal. Chem. 2018, 90, 440−458

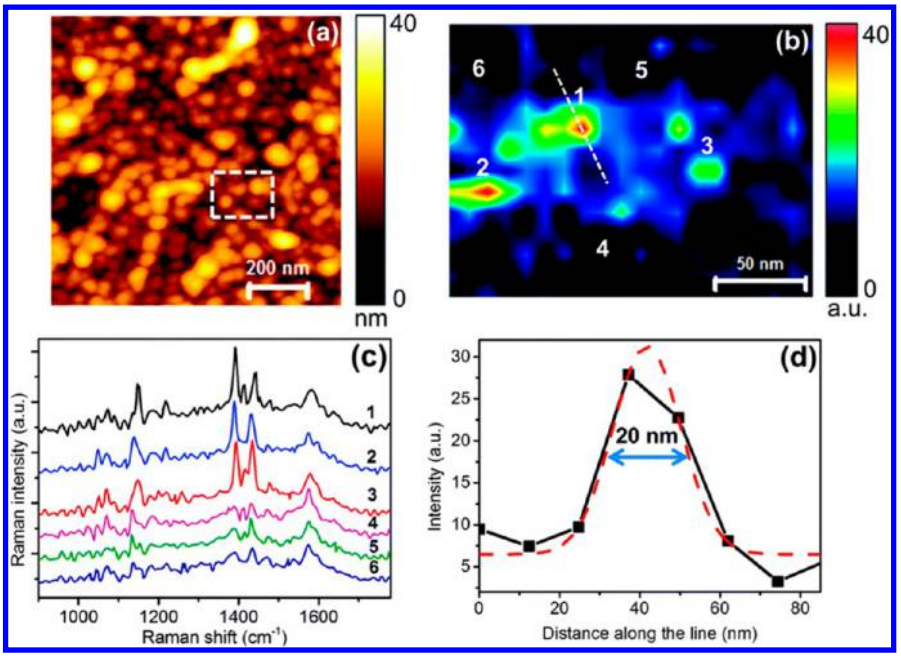

Figure 3. (a) AFM topography image of an Ag substrate with Ag nanoparticles on a glass substrate. (b) TERS map from the dashed rectangle marked in part a, showing the variation of the 1142 cm^{-1} Raman peak intensity of DMAB. (c) Near-field spectra from the positions marked in part b. Integration time: 0.5 s. (d) Intensity profile along the dotted line marked in part b showing the spatial resolution of the TERS map. Gaussian fit to the intensity profile is shown by the dashed red curve. Reproduced from Kumar, N.; Stephanidis, B.; Zenobi, R.; Wain, A. J.; Roy, D. *Nanoscale* **2015**, *7*, 7133−7137 (ref 103), with permission of The Royal Society of Chemistry.

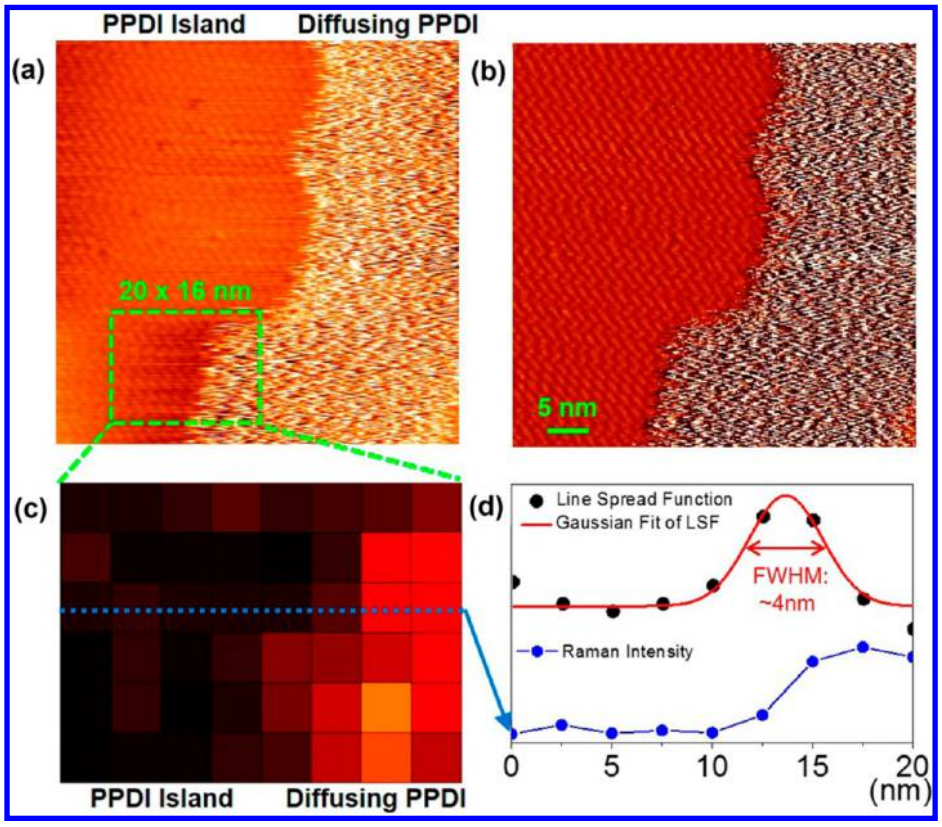

Figure 4. STM and TERS images of 2D dynamic phase boundary of PPDI on Ag(100). (a) STM topographic image and (b) STM current image (50 nm × 50 nm) measured with an Ag tip illuminated by a 1 mW continuous wave (CW) laser (λex = 532 nm). (STM imaging conditions: V = +1.5 V; I = 300 pA). (c) TERS mapping of the 1350 cm^{-1} Raman peak (8 pixels × 6 pixels, ∼2.5 nm per pixel, 10 s acquisition per pixel), processed from all individual TERS spectra acquired at each pixel. (d) TERS line scan shows ∼4 nm spatial resolution. Reproduced from Jiang, N.; Chiang, N.; Madison, L. R.; Pozzi, E. A.; Wasielewski, M. R.; Seideman, T.; Ratner, M. A.; Hersam, M. C.; Schatz, G. C.; Van Duyne, R. P. *Nano Lett.* **2016**, *16*, 3898−3904 (ref 106). Copyright 2016 American Chemical Society.

DOI: 10.1021/acs.analchem.7b04151
Anal. Chem. 2018, 90, 440−458

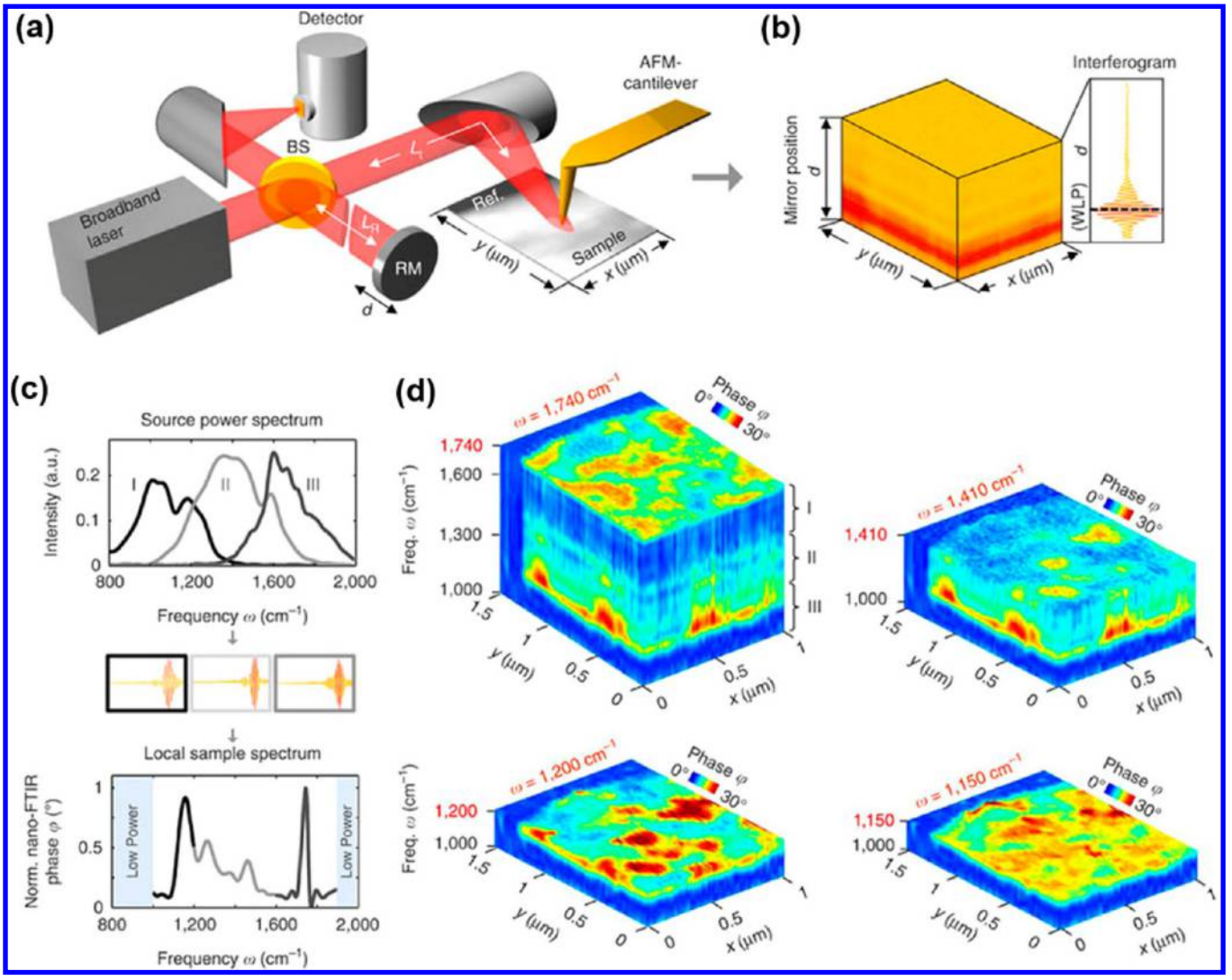

Figure 5. (a) Setup employing a mid-infrared laser continuum source for tip illumination. The tip scans the sample surface while at each pixel the light backscattered from the tip is analyzed with a Michelson interferometer that is operated as a Fourier transform spectrometer. The setup comprises a beam splitter (BS, uncoated ZnSe), a reference mirror (RM), and a detector. (b) 2D array of interferograms. (c) Top: Output spectra of the source. Middle: Interferograms recorded for each output spectrum. Bottom: Broadband nano-FT-IR spectrum composed by three nano-FTIR spectra obtained by Fourier transform of the corresponding interferograms and normalization to a reference spectrum (middle panel). (d) Hyperspectral infrared data cubes of spectral resolution of 35 cm^{-1}, cut at different frequencies ω. They show the normalized phase ϕ of the tip-scattered light as a function of position (x, y) and frequency ω. Reproduced by permission from Macmillan Publishers Ltd.: Nature Communications, Amenabar, I.; Poly, S.; Goikoetxea, M.; Nuansing, W.; Lasch, P.; Hillenbrand, R. *Nat. Commun.*, **2017**, *8*, 14402 (ref 118). Copyright 2017.

TERS.[103] In the study, TERS differentiated between catalytically active and inactive particles with 20 nm spatial resolution, as shown in Figure 3. Later, the Ren group spatially resolved the site-specific electronic and catalytic properties of a Pd/Au(111) bimetallic surface with 3 nm resolution.[104] These studies may pave the way for TERS to investigate heterogeneous catalysis at the nanoscale and lead to spectroscopic imaging of individual catalytic sites.

TERS presents unique advantages for probing single molecule dynamics under ultrahigh vacuum conditions. Using UHV-TERS at low temperature, Tallarida et al. observed the unique signature of single molecule isomerization in the form of anticorrelated flip-flops between cis and trans isomers.[105] Van Duyne and co-workers observed molecular orientations in a dynamic two-phase system at room temperature using UHV-TERS and STM, which were aided by time-dependent density functional theory simulations.[106] Interestingly, TERS provides complementary chemical information about PPDI molecules on areas where no meaningful STM topographic information can be obtained (Figure 4).

Recently, El-Khoury and co-workers have reported an interesting application of TERS to map the local electric fields.[107,108] By monitoring the plasmonic modes of strategically selected molecular reporters coated on an Ag (or Au) AFM tip, they were able to image plasmon-enhanced electric fields localized at nanometric features on a silver substrate.

IR s-SNOM

IR s-SNOM measures the scattered light from a sharp metallic AFM tip operating in tapping mode at the sample surface. In s-SNOM, the amplitude and phase of the detected signal are dependent on the tip-mediated light-sample interaction, and the signal is enhanced when the incident IR excitation matches vibrational modes in the sample. The spatial resolution of s-

DOI: 10.1021/acs.analchem.7b04151
Anal. Chem. 2018, 90, 440−458

SNOM imaging is typically dependent on the radius of the AFM tip, which is usually ~20 nm. s-SNOM does not detect light absorption like conventional IR spectroscopy but rather detects the scattered light. The observed signal is dependent on the local refractive index of the sample and the tip. The measured s-SNOM spectra may not correspond to the far-field IR absorption spectra, making chemical identification challenging. As a result, mathematical models are commonly needed to interpret the measured s-SNOM spectra.[109−113] In addition, interferometric techniques and phase-sensitive lock-in detection are required in s-SNOM to distinguish the near-field signal from the far-field scattering background. Comprehensive theories and instrumental details of s-SNOM can be found in previous review articles.[114,115] Despite the complex experimental setups, s-SNOM has been applied to characterize various samples due to its nanoscale spatial resolution (referred to as nano-FT-IR or IR nanospectroscopy). Here we review the most recent advances and applications of s-SNOM for spectroscopic imaging.

Technical Advances of s-SNOM. High brilliance and broadly tunable IR sources are needed for spectroscopic s-SNOM measurements. Quantum cascade lasers (QCLs) have been widely applied for IR s-SNOM because their high spectral irradiance, and their narrow tuning ranges (few hundreds of wavenumbers) are suitable for acquiring s-SNOM spectra and maps at vibrational modes of interest.[110,113,116,117] Recently, Hillenbrand and co-workers used a tunable bandwidth-limited laser continuum to achieve near-field infrared nanoscopy covering a spectral range from 1000 to 1900 cm^{-1}, by recording and stitching together multiple bandwidth-limited spectra (Figure 5).[118] Broader spectral ranges have also been achieved using a thermal emitter as a light source; however, the incoherent nature of the radiation and the associated low spectral irradiance is perceived as a limitation.[119] Lahneman et al. introduced a high temperature plasma light source that is both broadband and more brilliant in the infrared spectral region than conventional thermal light sources.[120] This plasma source was used to measure the near-field IR spectra of phonon resonances of SiO_2 and $SrTiO_3$. Very recently, s-SNOM was combined with IR synchrotron radiation, termed as synchrotron IR nanospectroscopy, which enables broadband molecular and phonon vibrational spectroscopic imaging with rapid spectral acquisition over the full mid-infrared (500−5000 cm^{-1}) region with nanoscale spatial resolution.[121−124]

As mentioned above, complex interferometric techniques are necessary in s-SNOM setup to amplify the near-field signal and determine its phase with respect to a known reference field. Hillenbrand and co-workers have reported a method for rapidly acquiring background-free, high-resolution, near-field spectra that combines the well-established pseudoheterodyne detection technique with a wavelength-swept QCL.[116] They modified the commonly used pseudoheterodyne detection scheme by operating the interferometer in the white light position, which was found to be critical for measurement repeatability. The Raschke group has presented a simplified symmetric geometry using the spatially coherent background scattered light from within the confocal sample volume as a reference field for signal amplification in both self-homodyne and self-heterodyne interferometry.[110] The simplified setup exhibited increased stability due to reduced sensitivity to fluctuations and drift, leading to shorter measurement times and more robust data collection. Wang et al. reported a near-field signal extraction method that enables the use of low-repetition-rate pulsed light sources, which are usually incompatible with the lock-in detection mechanism that is required for s-SNOM.[117] This method correlates scattering signals from the pulses with the mechanical phases of the oscillating s-SNOM probe to obtain the near-field signal and enables s-SNOM with high peak-powers that facilitate nanoscale spectroscopic investigations.

Recently, Kajihara and co-workers reported a new setup called passive s-SNOM, in which thermally excited fields are detected without an external light source.[125,126] They demonstrated the capability of passive s-SNOM by measuring thermally excited surface evanescent waves on Au/SiO_2 gratings in the long-wavelength infrared region.[126] Other technical advances have focused on incorporating s-SNOM with other imaging modalities to realize correlative multimodal imaging. Several research groups have incorporated s-SNOM with AFM-based force spectroscopy for correlated infrared nanospectroscopic and nanomechanical imaging of various materials such as polymers, biomolecules, and nanomaterials.[127−129] In addition, the combination of ultrafast pump−probe spectroscopy with s-SNOM has been demonstrated to achieve spatiotemporal spectroscopic imaging with nanometer spatial resolution and femtosecond temporal resolution.[130−133]

Applications of s-SNOM. *s-SNOM in Materials Science.* Polaritons in two-dimensional (2D) van der Waals materials exhibit hyperbolic dispersion and strong field confinement, which makes them highly attractive for applications including optical nanofocusing, sensing, and control of spontaneous emission. s-SNOM has been heavily applied to probe these surface polaritons in layered 2D materials such as graphene and graphene-like hexagonal boron nitride (hBN).[111,112,134−137] A recent work by Basov and co-workers presented the direct experimental access to the hyperbolic phonon polaritons that are effectively modulated in a graphene/hBN heterostructure, using s-SNOM based nano-IR spectroscopy and imaging.[134] Almost simultaneously, Deneke and co-workers investigated graphene/hBN plasmon−phonon coupling and plasmon delocalization, showing that broadband IR s-SNOM is able to distinguish between the graphene/hBN and the graphene/SiO_2 heterostructures as well as differentiate between graphene stacks with different numbers of layers.[135] The Wang group at Berkeley has imaged phonon polaritons in hBN crystals[111] and, more recently, investigated the edge-reflection of two-dimensional surface polaritons in graphene sandwiched in hBN flakes,[136] using amplitude- and phase-resolved s-SNOM imaging. Very recently, Bezares et al. applied s-SNOM to study highly doped graphene and interestingly observed strong coupling between intrinsic graphene phonons and plasmons.[138] Other than the 2D materials, one-dimensional boron nitride nanotubes have also been studied by correlative near-field nanomechanical and nano-IR spectroscopic measurements.[129] Using multimodal characterization, the IR signatures and mechanical responses of structural defects in individual boron nitride nanotubes have been correlated.

A number of other materials have also been characterized by s-SNOM. Levratovsky and Gross reported nanoscale chemical mapping of the catalytic reactivity of OH-functionalized N-heterocyclic carbene molecules on platinum nanoparticles.[139] Johnson and Bohmler used s-SNOM to monitor the atmospheric corrosion of a copper surface, and spectroscopically determined different corrosion products and their spatial distribution with 20 nm resolution.[140] Ayache et al. used IR s-SNOM to study the chemical composition of the solid

DOI: 10.1021/acs.analchem.7b04151
Anal. Chem. 2018, 90, 440−458

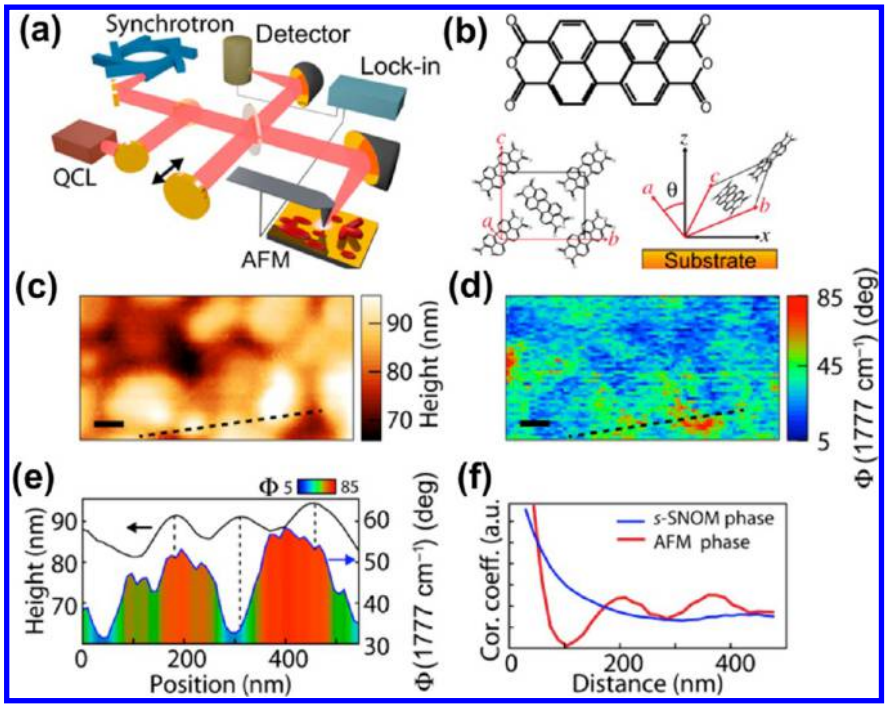

Figure 6. (a) Schematic of IR s-SNOM using both synchrotron and QCL radiation. (b) Lewis structure (top) and crystal structure (bottom) of PTCDA in the β phase. (c) Topography and (d) s-SNOM phase Φ_{NF} ($\bar{\nu}$) images of PTCDA. Scale bars, 100 nm. (e) Line cut of AFM height and Φ_{NF} ($\bar{\nu}$) along the dashed transect indicated in parts c and d, showing that molecular orientation is uncorrelated with topographic features. (f) Radial correlation function (red) of the AFM tapping phase, indicating the presence of 3D islands with characteristic size and spacing and Φ_{NF} ($\bar{\nu}$) (blue), which shows an extended correlation length of crystallite orientation. Reproduced from Muller, E. A.; Pollard, B.; Bechtel, H. A.; van Blerkom, P.; Raschke, M. B. **2016**. Infrared vibrational nanocrystallography and nanoimaging. *Science Advances*, *2*(10), p.e1601006 (ref 143), under Creative Commons License.

electrolyte interphase on Li-ion negative electrodes at the length scale of its basic building blocks, revealing significant chemical variation tied to specific topographic features.[141] Using nano-IR spectroscopic techniques based on s-SNOM and AFM-IR, Khanikaev et al. visualized the origin of circular dichroism in two-dimensional metamaterials, showing it is related to nonradiative dissipation of the constituent meta-molecules that occurs on the nanoscale.[142]

Recently, the Raschke group presented an interesting application of IR s-SNOM for optical nanocrystallography and nanoimaging. Structural heterogeneity of polycrystalline perylenetetracarboxylic dianhydride (PTCDA), including orientation distributions and correlations across domain boundaries and morphological features, was characterized using IR vibrational nanocrystallography (Figure 6).[143] Liu et al. have applied s-SNOM to study a variety of vanadium dioxide (VO_2) crystalline forms, including bulk single crystals and oriented thin films, and showed that epitaxial strain in VO_2 thin films leads to intermediate electronic and lattice states that are intrinsically different from those found in bulk.[144] On a spatially heterogeneous polytetrafluoroethylene molecular model system, Atkin et al. demonstrated femtosecond s-SNOM to observe ultrafast coherent dynamics of molecular subpopulations that define the properties of many functional materials.[145]

s-SNOM in Life Science. IR-based s-SNOM has also recently been applied for nanoscale chemical imaging of biological samples. Using probe-based s-SNOM in conjunction with tunable QCL diode lasers, Phillips and co-workers obtained chemical maps inside single cells with spatial resolution 1000× better than the diffraction limit.[146] Qin et al. investigated the electron irradiation-regulated structural transitions of silk fibroin protein with molecular level resolution by monitoring the IR signal of amide I and II bands using both AFM-IR and s-SNOM.[147] These amide bands contain information about protein secondary structures and are also used for nanoimaging of proteins and their structural changes in other biological samples, such as the distribution of melanin granules in human hair,[118] amyloid-like ribbons of amelogenins in enamel mineralization,[148] and collagen fibrils in damaged human tendons.[149]

To date, most s-SNOM applications of biological systems have been performed on dried samples. It is desirable, though challenging, to demonstrate spectroscopic s-SNOM in biologically relevant solutions. Recently, Khatib et al. reported a graphene-based liquid cell platform for near-field IR nanospectroscopy of the tobaccomosaic virus (TMV) in aqueous environments.[150] In this work, large-area graphene acts as an impermeable monolayer barrier that allows for nano-IR inspection of underlying molecular materials in the liquid, while the AFM probe is operated in air. Using this configuration, the researchers successfully resolve individual virus particles by measuring the amide bands of TMV. This work demonstrated the potential of s-SNOM for nano-IR investigation in aqueous solutions, however, the ultrathin graphene liquid cells used is not easy to implement and warrant further studies to apply s-SNOM in liquid.

AFM-IR

AFM-IR, also known as photothermal induced resonance (PTIR), is a novel technique that allows IR spectroscopic imaging with a spatial resolution far beyond the diffraction-limited IR microspectroscopy. A typical AFM-IR setup consists

DOI: 10.1021/acs.analchem.7b04151
Anal. Chem. 2018, 90, 440−458

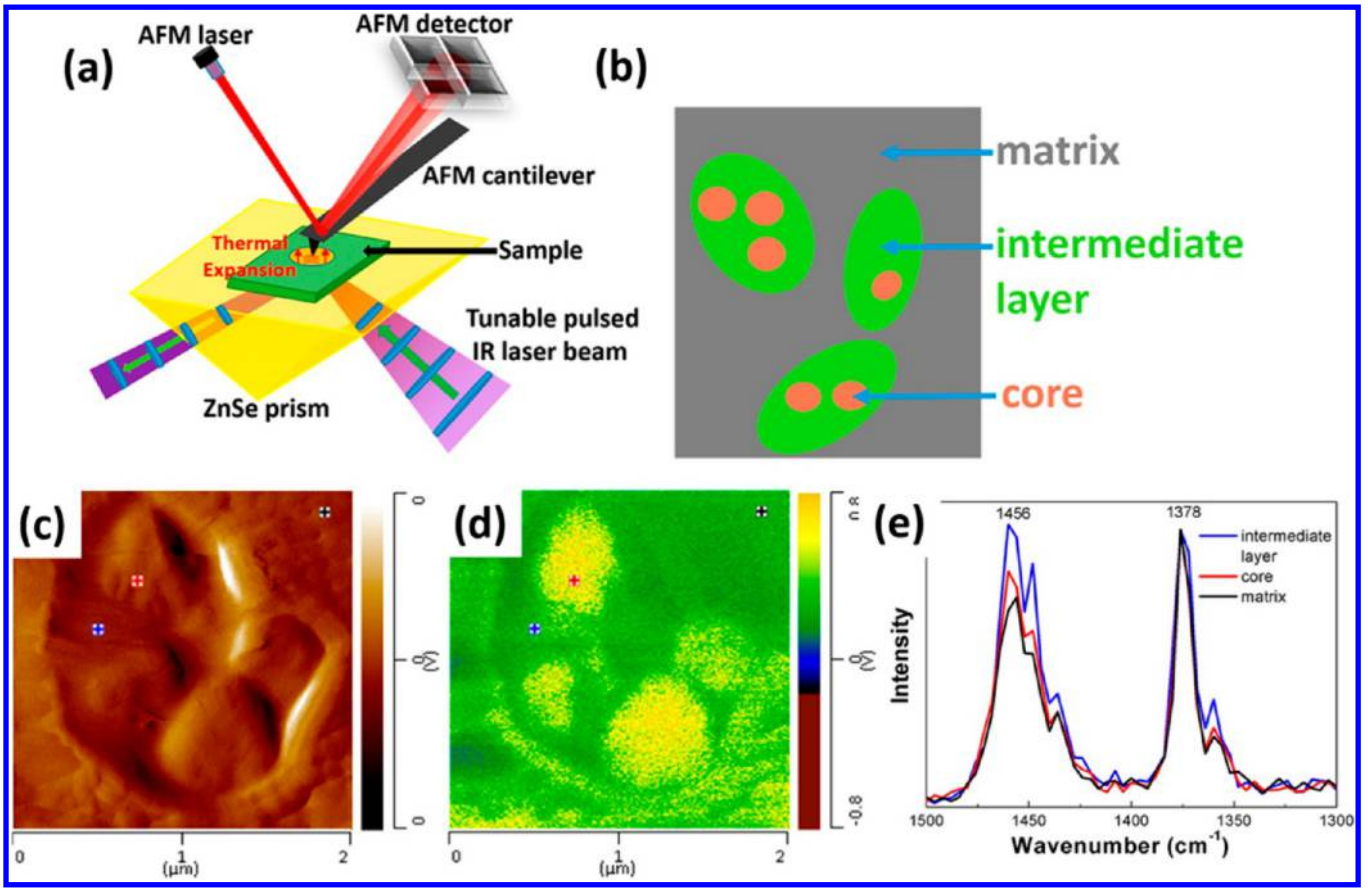

Figure 7. Schematic illustration of the AFM-IR setup (a) used to analyze the composition of nanodomains in HIPP (b). (c) AFM height image and (d) AFM-IR map of the methyl symmetric C−H bending at 1378 cm^{-1}. (e) AFM-IR spectra taken at the locations marked in parts c and d, normalized to the 1378 cm^{-1} band, indicative of different ethylene contents as shown by the intensity of the 1456 cm^{-1} band. Reproduced from Tang, F.; Bao, P.; Su, Z. *Anal. Chem.* **2016**, *88*, 4926−4930 (ref 169). Copyright 2016 American Chemical Society.

of a pulsed wavelength-tunable light source for sample irradiation and an AFM tip in contact with the sample to detect the local thermal expansion resulting from the absorption of light (Figure 7). AFM-IR spectra correlate very well with conventional FT-IR spectra, making them simple to apply for chemical analysis. The first AFM-IR experiment was demonstrated by the Dazzi group in 2005.[151] The technique has evolved over the past decade and a variety of applications have been reported. More details about the technique can be found in previous review articles.[115,152] Here we review the most recent advances and applications of AFM-IR.

Technical Advances of AFM-IR. In early AFM-IR experiments, the optical parametric oscillator (OPO) tunable laser source with relatively low repetition rate (1 kHz) was used, which required the cantilever oscillation to ring down at its natural resonance frequencies after each laser pulse. Recently, Belkin and co-workers replaced the OPO laser source with a variable repetition rate QCL, and presented a dramatic improvement in the AFM-IR signal.[153] They tuned the QCL repetition rate to match AFM cantilever's contact resonance frequency, which leads to a large increase in the oscillation amplitude and changes the ring-down oscillation to a continuous oscillation. This technique is now recognized as resonance enhanced AFM-IR (RE-AFM-IR) and significantly improves the sensitivity compared to the original AFM-IR technique. Using RE-AFM-IR, several research groups have demonstrated nanoscale IR imaging of polymers[153−156] and biomembranes[157−159] with sensitivity down to monolayers. Benefiting from the improved sensitivity, time-resolved RE-AFM-IR experiments, monitoring the structural changes in poly-L-lysine, have been performed with a temporal resolution of 15 s per spectrum over a spectral range of more than 100 cm^{-1}.[155] It should be noted that the contact resonance of the AFM cantilever is dependent on the properties of materials in the sample. When performing an imaging experiment on a heterogeneous sample, it is complicated to match the contact resonance and the excitation frequency for all pixels in an image. Lendl and co-workers demonstrated how an incorrect excitation frequency in RE-AFM-IR experiments results in imaging artifacts arising from changes in the contact resonance frequency instead of the chemical composition.[160] To solve this, Lendl et al. proposed a controller design that continuously tracks and readjusts the excitation frequency to match the AFM resonance frequency. Very recently, Belkin and co-workers reported the first RE-AFM-IR experiment when the sample and the scanning probe are completely immersed in water.[156] This technique has successfully imaged polymer samples with 25 nm spatial resolution in the biologically relevant amide spectral regions.

To take full advantages of the chemical analysis capability of AFM-IR, bright IR sources with wide spectral range are preferred. Recently, Cinque and co-workers reported the first use of infrared synchrotron radiation (IR-SR) as a broadband source for RE-AFM-IR.[161] Taking advantage of the bright and broadband nature of IR-SR, a spectrum was collected from the near-IR up to the far-IR range within 15 min. Further

DOI: 10.1021/acs.analchem.7b04151
Anal. Chem. 2018, 90, 440−458

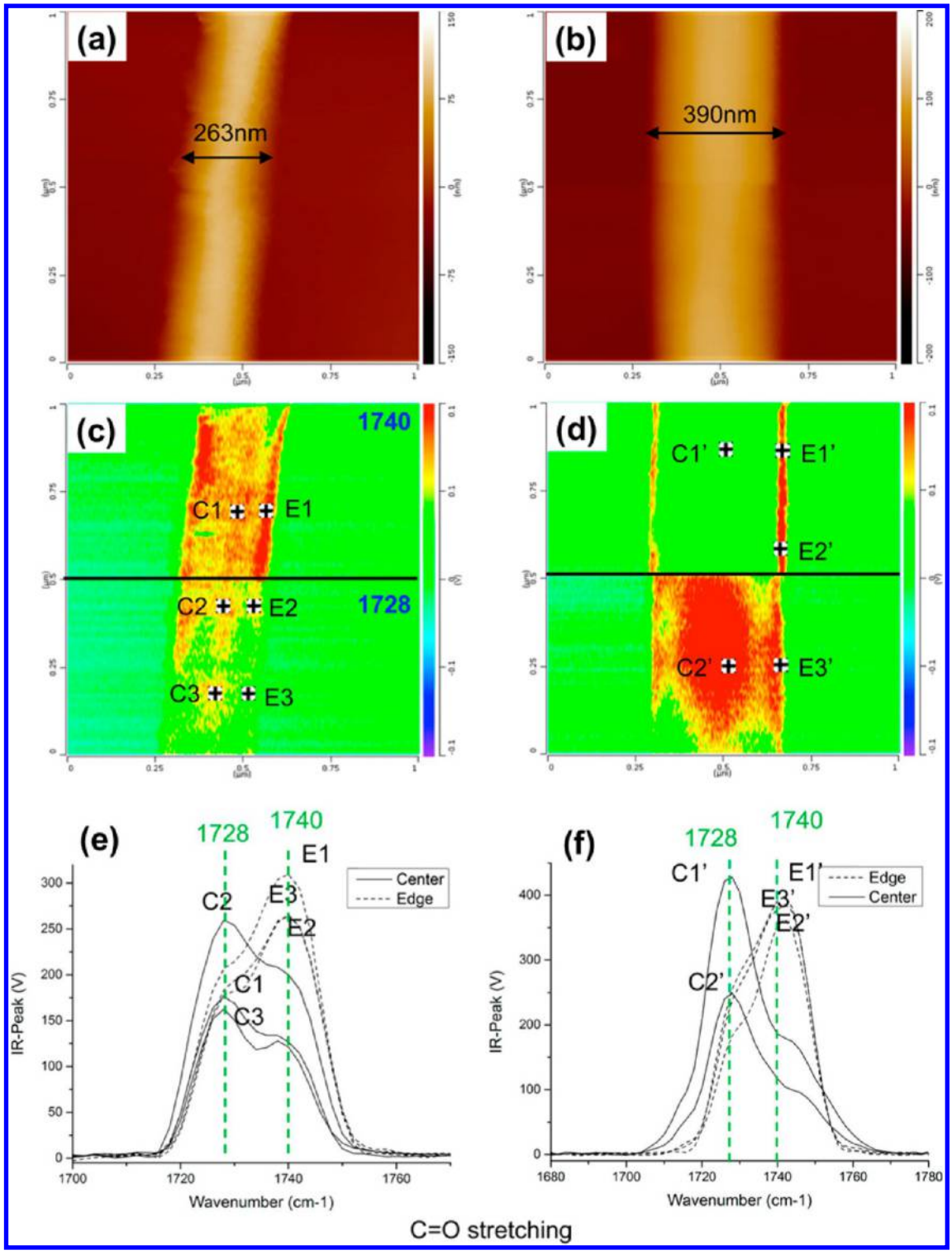

Figure 8. AFM height images (a, b), IR peak images (c, d), and AFM-IR spectra (e, f) of two single electrospun PHBHx fibers. For each IR image, the upper half was recorded at 1740 cm^{-1} and the lower half at 1728 cm^{-1}. The black spots in parts c and d indicate the position of the AFM tip when collecting the AFM-IR spectra. The appearance of the β-crystalline phase is indicated by the characteristic IR absorption peak at 1740 cm^{-1} in the IR spectrum. The IR absorption peak at 1728 cm^{-1} is characteristic of the α-crystalline phase, which is the thermodynamically stable crystal structure of PHBHx. Reproduced from Gong, L.; Chase, D. B.; Noda, I.; Marcott, C. A.; Liu, J.; Martin, D. C. Ni, C.; Rabolt, J. F. *Macromolecules* **2017**, *50*, 5510−5517 (ref 179). Copyright 2017 American Chemical Society.

improvements in imaging speed are needed in order to apply IR-SR AFM-IR for collecting images of hundreds or more pixels. In another study, Centrone et al. have presented the extension of AFM-IR spectral range in the visible and near IR range, by incorporating three OPO lasers with different spectral ranges into a commercial AFM-IR setup.[162] They successfully demonstrated the acquisition of absorption spectra and maps over wavelengths from 500 nm to 16.0 μm with approximately 20 nm spatial resolution independent of excitation wavelength.

DOI: 10.1021/acs.analchem.7b04151
Anal. Chem. 2018, 90, 440−458

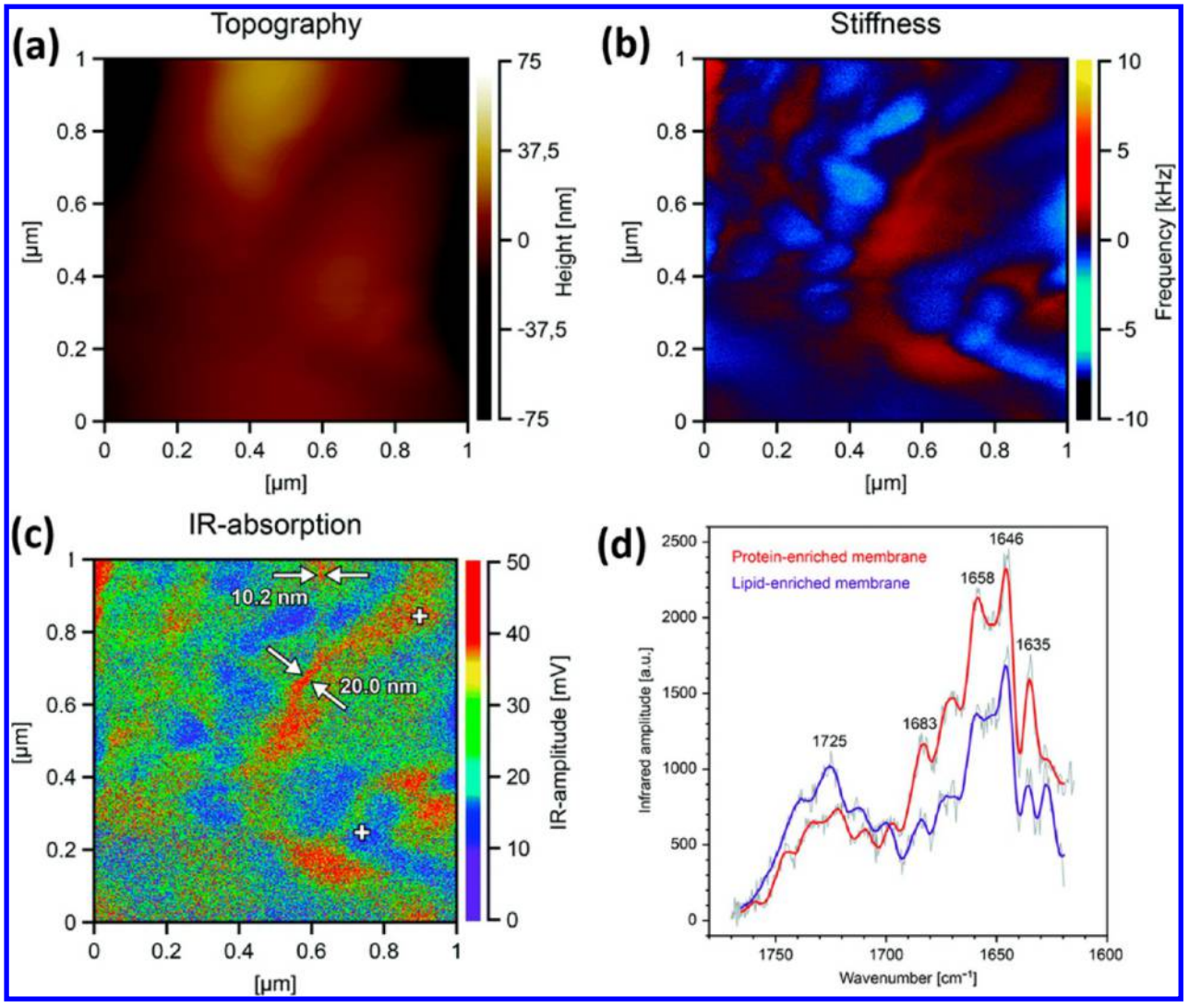

Figure 9. (a) Surface topography, (b) mechanical-stiffness map, and (c) IR-absorption pattern of the lipoprotein multibilayer recorded simultaneously on 1 μm × 1 μm area of the sample, the thickness of which was approximately 1.2 μm. (d) IR-absorption spectra of the lipoprotein multibilayer. The spectra were recorded at the positions denoted with white crosses in part c: the trace drawn in red (protein-enriched membrane) corresponds to the cross in the upper portion of the image and the one drawn in violet (lipid-enriched membrane) to that in its lower portion. The spectra were recorded in the amide-I region of the protein wavenumber range (1600−1700 cm^{-1}) and in the ester carbonyl stretching region of the lipid components' wavenumber range (1700−1750 cm^{-1}). Reproduced from Gruszecki, W. I.; Kulik, A. J.; Janik, E.; Bednarska, J.; Luchowski, R.; Grudzinski, W.; Dietler, G. *Nanoscale* **2015**, *7*, 14659−14662 (ref 191), with permission of The Royal Society of Chemistry.

AFM-IR has also been integrated with other imaging modalities to obtain complementary information about the sample. Lo et al. combined AFM-IR with contact resonance AFM to perform nanoscale chemical-mechanical characterization of low-k dielectrics.[163] Vitry et al. used AFM-IR together with mode synthesizing AFM for three-dimensional chemical imaging of lipid production in bacteria with sub-50 nm spatial resolution.[164] Latour et al. correlated AFM-IR with second harmonic generation to monitor collagen denaturation to gelatin.[165]

Recently, Katzenmeyer et al. introduced scanning thermal infrared microscopy (STIRM), which can obtain IR spectra and maps with nanoscale spatial resolution.[166] By directly measuring the temperature change caused by IR light absorption at the sample, STIRM can complement the chemical imaging capability of AFM-IR for materials with a small thermal expansion coefficient. Wang et al. developed peak force infrared (PFIR) microscopy, which enables spatial imaging of IR absorption responses with a spatial resolution of ∼10 nm and simultaneous nanoscale mapping of mechanical properties.[167] PFIR operates in the peak force tapping mode of AFM, which is robust on various rough and sticky sample surfaces that are not suitable for the contact mode used in typical AFM-IR measurements.

Applications of AFM-IR. *AFM-IR in Polymer Sciences.* AFM-IR has been heavily applied in characterizing polymers. It provides the extraordinary capability to characterize the chemical identities, map the nanoscale compositional domains, and even track the dynamic changes of various polymeric materials.

One popular application of AFM-IR is to analyze the composition and distribution of components in composite polymeric materials. Brown and Bhushan reported a method for preparing leophobic polymer−nanoparticle composite nanomaterials.[168] In their work, AFM-IR was used to analyze the distribution of polycarbonate and confirm that the

DOI: 10.1021/acs.analchem.7b04151
Anal. Chem. 2018, 90, 440−458

nanoparticle agglomerates are embedded in the polymer surface. Tang et al. applied AFM-IR to quantitatively determine the compositions of different phase domains in high-impact polypropylene (HIPP).[169] Using calibration spectra generated by conventional FT-IR, they were able to perform quantitative analysis of the chemical composition of nanoscopic domains in HIPP samples (Figure 7). Kelchtermans et al. presented the characterization of a polyethylene-polyamide multilayer film using AFM-IR, demonstrating its capability to obtain nanoscale spectroscopic, thermal, and mechanical property differences in the tie layers located between the individual polyethylene and polyamide layers of a multilayer cling film of initially unknown structure.[170] AFM-IR has also been applied to analyze the chemical structures of composite materials, such as hybrid rubbers composed of polyamide and hydrogenated acrylonitrile butadiene,[171] polycaprolacton-chitosan nonwovens,[172] and paclitaxel/chitosan coassembled core−shell nanofibers.[173]

The Remita group at University of Paris-Sud reported novel synthesis methods for different conducting polymers such as poly(3,4-ethylenedioxythiophene)[174,175] and poly(diphenylbutadiyne),[176,177] which have various potential applications in energy conversion and storage. In these studies, AFM-IR characterized the synthesized polymeric nanostructures, as it allows chemical identification of the polymer nanostructures simultaneously with morphological characterization. A series of impressive AFM-IR studies have been reported by Rabolt and co-workers, in which they investigated the structure of electronspun fibers made of Poly[(R)-3-hydroxybutyrate-*co*-(R)-3-hydroxyhexanoate] (PHBHx).[178,179] AFM-IR spectra and imaging of single nanofibers revealed a heterogeneous core−shell spatial distribution of two crystalline polymorphs of PHBHx, the thermodynamically stable α-form and the metastable β-form (Figure 8).[179]

AFM-IR has also been used to investigate the miscibility of different drug-polymer blends and characterize the size and compositions of specific domains.[180,181] For example, Li and Taylor investigated the miscibility behavior of telaprevir, a poorly water-soluble drug, with three different polymers, HPMC, HPMCAS, and PVPVA, at different drug to polymer ratios where phase separation takes place.[181] AFM-IR images showed clear contrast between the polymer-rich continuous domains and the drug-rich discrete domains ranging from below 50 nm to a few hundred nanometers. The direct visualization of the structure and chemical composition of phases provides valuable insights in the miscibility of pharmaceutical components.

Using AFM-IR, it is possible to track dynamic compositional changes in materials. In the past few years, Morsch and co-workers have made tremendous progress unraveling the degradation mechanism of intact organic coatings.[182−186] Researchers mapped local water uptake in epoxy-phenolic coatings under different conditions with nanoscale lateral resolution[182−184] as well as correlated the internal cross-linking density to the appearance of nanoscale chemical heterogeneities in epoxy networks.[182,185,186] In a recent study, Morsch et al. observed the direct evidence for locally induced photocatalytic degradation in the vicinity of anatase titanium white pigments at the surface of linseed oil paints.[187] Other related studies include the characterization of collagen degradation in ancient parchments using AFM-IR in combination with nonlinear optical microscopy.[165]

AFM-IR in Life Sciences. AFM-IR has been widely applied for chemical imaging of subcellular heterogeneity in single cells and bacteria with a typical spatial resolution of 50−100 nm, by monitoring the specific IR absorption bands of cellular components such as proteins and lipids.[157,164,188−190] For example, Giliberti et al. have presented the application of AFM-IR to study the protein clustering in chemically stressed HeLa cells using the amide-I vibrational mode at 1660 cm^{-1}.[190] Interestingly, Gruszecki et al. reported the AFM-IR imaging of protein-containing lipid membranes with a resolution better than 20 nm.[191] The observed resolution was attributed partially to the different mechanical properties and thermal conductivity of the lipid and protein components (Figure 9). A few recent studies have demonstrated the capability of AFM-IR to chemically monitor biological processes within the cells. The Dazzi group used AFM-IR to investigate the production of poly(hydroxybutyrate) (PHB) within a single bacteria.[192] By monitoring the local changes in the IR signal, they estimated the degree of crystallinity for native PHB within bacteria without any extraction and purification steps. Wang et al. correlated AFM-IR and nanoindentation measurements to characterize the chemical and mechanical properties of the cell wall in wood interacting with phenol-formaldehyde resin.[193] In an AFM-IR study of bacteria on a polymer film, Barlow et al. demonstrated that the chemical sensitivity of AFM-IR can be affected by the sample materials, and corrections are required for quantitative analyses.[194]

Another popular application of AFM-IR in life science is to study the secondary structures of proteins and peptides,[147,195−197] as well as their aggregates, namely, amyloid fibrils associated with neurodegenerative diseases like Huntingtons and Alzheimers.[198−201] Khanal et al. used AFM-IR to study the interactions between proteins and nanoparticles.[195] Measuring the amide I and amide II absorption bands provides conformational information on the proteins during protein−particle interactions, suggesting implications for nanomaterial toxicity in biological environments. Paluszkiewicz et al. investigated cataract development in the human lens with AFM-IR, in which disease development was associated with the secondary structure of proteins.[196] Ruggeri et al. applied AFM-IR to study the misfolding and aggregation of the Josephin domain of ataxin-3, implicated in spinocerebellar ataxia-3.[198] Taking advantage of the high chemical sensitivity and spatial resolution of AFM-IR, they monitored the conversion of monomers into amyloid β-sheet aggregates and linked the stiffness of amyloid structures to their β-sheet content at molecular level. In another recent work, the same research group studied the fibril aggregates of the first exon of the Huntington protein (Exon1), correlating morphological and mechanical properties of Exon1 aggregates with their structural organization at the single-molecule and nanometer scale.[199] These recent reports demonstrated the usefulness of AFM-IR to investigate the structural bases of protein fibrillization and misfolding, providing a deeper understanding of protein aggregation.

Other AFM-IR Applications. In addition to the most popular applications in polymer and life sciences, AFM-IR has seen novel applications in other areas recently. For example, AFM-IR has been applied to characterize nanoscale chemical structures of low-k dielectrics.[163,202] A series of collaborative studies by the Huang group at University of Nebraska-Lincoln and the Centrone group at National Institute of Standards and Technology used AFM-IR to investigate the compositional changes of perovskite solar cells during various processes.[203−206] Furthermore, the Centrone group has utilized

DOI: 10.1021/acs.analchem.7b04151
Anal. Chem. 2018, 90, 440−458

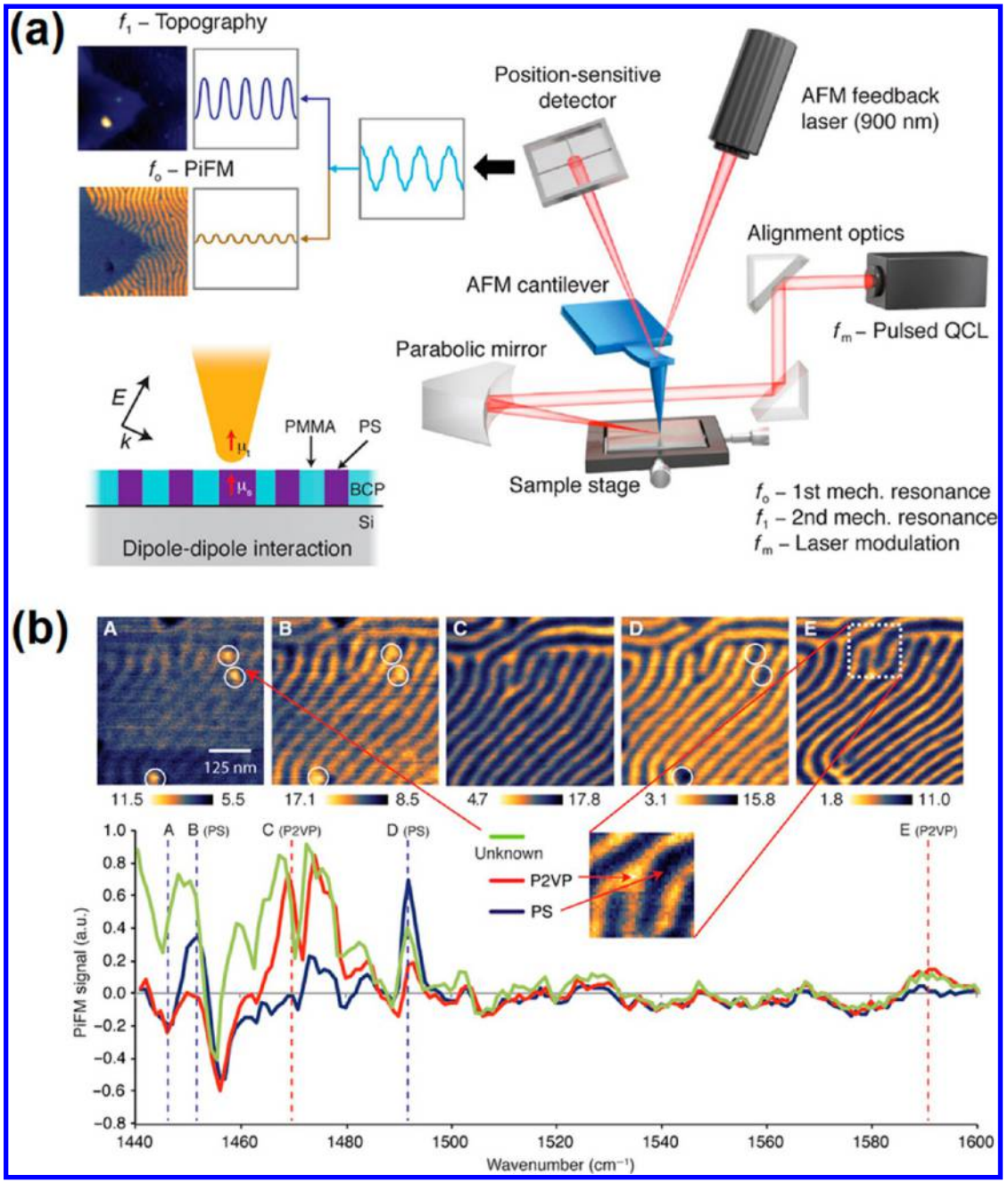

Figure 10. (a) Schematic of an IR PiFM experiment. The incident mid-IR laser is electrically triggered to pulse at $f_m = f_1 - f_0$, where f_0 and f_1 are the first and second mechanical eigenmode resonances of the cantilever. (b) Chemical imaging of PS-*b*-P2VP fingerprint patterns. PiFM imaging at (A–E) 1447 cm^{-1}, 1452 cm^{-1}, 1469 cm^{-1}, 1492 cm^{-1}, and 1589 cm^{-1}. The PiFM point spectra taken from the locations shown in parts A, B, and E were normalized against a Si background. Reproduced from Nowak, D., Morrison, W., Wickramasinghe, H. K., Jahng, J., Potma, E., Wan, L., Ruiz, R., Albrecht, T. R., Schmidt, K., Frommer, J., and Sanders, D. P., **2016**. Nanoscale chemical imaging by photoinduced force microscopy. *Science Advances*, 2(3), p.e1501571 (ref 220), under Creative Commons License.

AFM-IR to map the distribution and intensity of surface-enhanced infrared absorption hot-spots in plasmonic resonators.[207−209]

PiFM

PiFM is an emerging technique that enables spectroscopic imaging of materials with nanoscale resolution. Theoretical studies report that PiFM probes the dipole−dipole interaction forces between a metallic AFM tip and the induced dipoles in the sample. The induced dipole in the sample is dependent on the photoinduced polarization in the sample and therefore provides spectroscopic constrast.[210,211] In addition, since the photoinduced forces are highly localized at the tip−sample interface, PiFM typically exhibits a spatial resolution around ∼10 nm.[212] PiFM incorporates an AFM in noncontact/tapping mode, where the feedback is established at one mechanical resonance of the cantilever (f_0), and the high-contrast image is detected at another mechanical resonance (f_1) with a pulsed excitation laser modulated at a frequency equal to the difference between these two resonances ($f_m = f_1 - f_0$).[213,214] This heterodyne detection is reported to improve imaging contrast, as compared to direct detection at the modulation frequency

DOI: 10.1021/acs.analchem.7b04151
Anal. Chem. 2018, 90, 440−458

(f_m) and effectively avoid artifacts caused by photothermal effects.[215] Figure 10 shows a general schematic of PiFM experimental setup. More theoretical details and early experiments of PiFM are summarized in previous reports.[212,214] In this section, we review the most recent advances and applications of PiFM.

Depending on the optical excitation frequencies (from visible to mid-IR), PiFM can be used to image electronic or vibrational transitions in a sample. Recently, a number of studies have been carried out to probe different electronic properties via visible and near-IR excitations.[216−219] Jahng et al. reported the nanoscale visualization of the electric field distributions associated with propagating surface-plasmon polariton modes on flat gold surfaces, based on the detection of the photoinduced gradient force exerted by the evanescent field onto a sharp and polarizable tip.[216] Ambrosio and co-workers used PiFM to image the local refractive index contrast of a sample specifically designed to unambiguously decouple morphology from optical response with resolution better than 10 nm.[217] Huang et al. demonstrated PiFM can map the spatial electric field distributions of tightly focused laser beams with linear, radial, and azimuthal polarizations by measuring the optical force between a gold coated AFM probe and its image dipole on a glass substrate.[218] In another study, Tumkur and co-workers applied PiFM to characterize heterogeneities of plasmonic nanostructures by measuring the near-field optical forces and suggested that the enhancement of the detected forces follows the expected plasmonic field enhancements with strong polarization sensitivity.[219]

By moving the excitation wavelength to mid-IR range, PiFM can provide high-contrast images of different vibrational modes, which can be used to determine chemical species in a sample. Recently, Nowak et al. presented a study using PiFM to spatially map nanoscale patterns of individual chemical components of two different types of self-assembled block copolymer films, including PS-*b*-P2VP polymer (Figure 10).[220] In another example, hyperspectral PiFM was applied to map the optical patterns of P3HT films with sub-10 nm spatial resolution.[221]

PiFM has also been applied to probe nonlinear optical processes. Jahng et al. demonstrated the feasibility of probing the ultrafast nonlinear optical response of nanoscopic materials in a nonoptical manner by combining PiFM with ultrafast pump−probe spectroscopy.[222] The time-resolved PiFM suppresses the impact of the optical background that is intrinsic to conventional optical pump−probe techniques. Nonlinear vibrational characterization has also been probed with PiFM. Tamma et al. demonstrated the stimulated Raman spectroscopy and nanoscopy of molecules excited and measured only using near-field photoinduced forces without the need for far-field optical spectroscopic detection.[223,224] The detected Raman spectra were found to agree well with references. These experiments demonstrate the potential of PiFM to probe nonlinear electronic and vibrational transitions with single-molecule sensitivity.

Recently, Kim et al. reported the use of quartz tuning fork (QTF) as a probe for multifrequency PiFM,[225] instead of the commonly used cantilever tip, which is prone to the unwanted jump-to-contact problem under ambient conditions. In this report, distinct eigenmodes of a QTF system were fully characterized by simulations and experiments. Furthermore, by using the QTF in different configurations, the researchers demonstrated the usefulness of QTF to independently register the photoinduced forces in the axial (tapping) direction as well as in the lateral (shear force) direction, which is not easily attained with a cantilevered tip.

SUMMARY AND OUTLOOK

The rapid development of nanoscale spectroscopic imaging has been impressive in recent years. The incorporation of new hardware has produced new techniques, and the competition between commercial companies appears to be resulting in instruments with increasing accessibility for nonexperts. Today it is common for the instrument manufacturers to setup demonstrations at conference exhibitions and travel with functioning instruments. The current challenge appears to be choosing which flavor of nanospectroscopic imaging will address a specific research problem. There are clearly certain samples that are exemplars for each technique, such as carbon nanotubes and 2D materials in TERS or phase separated polymer blends for AFM-IR.

The ability to investigate samples in solutions remains experimentally challenging and will be an area to watch in the future. TERS has benefitted from the longest development time; however, the rapid growth of infrared-based approaches cannot be ignored. It appears that Raman-based detection and the ability to use visible light for excitation may benefit TERS and possibly PiFM, but the development of QCLs and tunable infrared lasers may overcome the power attenuation in aqueous environments.

TERS has demonstrated subnanometer spatial resolution and recent demonstrations in solution appear promising; however, there are still unresolved questions about mode selectivity that may limit the utility in certain applications that might be better addressed by the emerging methods.

Nonetheless, the ability to probe and image single molecules and address how the spatial context of the molecule affect the chemical behavior appears to be in the realm of the doable. It is expected that the field will see an increase in publications using nanoscale spectroscopic imaging in the coming years.

AUTHOR INFORMATION

Corresponding Author

*E-mail: Schultz.41@nd.edu.

ORCID

Zachary D. Schultz: 0000-0003-1741-8801

Notes

The authors declare no competing financial interest.

Biographies

Lifu Xiao received his Ph.D. in Biological Engineering from Utah State University in 2015. His dissertation research focused on developing spectroscopic and microscopic methods for sensing and imaging of mammalian cells and cell membrane receptors. He is currently a postdoctoral researcher in Professor Schultz's lab at University of Notre Dame, where his current research focuses on the investigation of protein−ligand interaction using surface- and tip-enhanced Raman spectroscopy in combination with chemometric methods.

Zachary D. Schultz earned is B.S. degree from the Ohio State University in 2000 and Ph.D. from the University of Illinois at Urbana−Champaign in 2005. Upon completing his Ph.D., he performed postdoctoral research at the National Institute of Standards and Technology (USA) and National Institutes of Health. Dr. Schultz began his independent career as an assistant professor of chemistry and biochemistry at the University of Notre Dame in 2009 and was

DOI: 10.1021/acs.analchem.7b04151
Anal. Chem. 2018, 90, 440−458

promoted with tenure to associate professor in 2015. Prof. Schultz holds a concurrent appointment in the Department of Chemical and Biomolecular Engineering at Notre Dame. Prof. Schultz's research at Notre Dame has focused on developing innovative approaches utilizing nanostructures for near field imaging and ultrasensitive label-free spectroscopic detection. Ultimately, the Schultz lab wants to push the limits of sensitivity and spatial resolution of label-free detection for applications in biological and interfacial systems.

■ ACKNOWLEDGMENTS

The authors acknowledge support from the National Institute of General Medical Sciences, part of the U.S. National Institutes of Health, Award R01GM109988, and the National Science Foundation Award CHE-1507287.

■ REFERENCES

(1) Abraham, J. L.; Etz, E. S. *Science* **1979**, *206*, 716−718.
(2) Sweedler, J. *Crit. Rev. Anal. Chem.* **1993**, *24*, 59−98.
(3) Lewis, E. N.; Treado, P. J.; Reeder, R. C.; Story, G. M.; Dowrey, A. E.; Marcott, C.; Levin, I. W. *Anal. Chem.* **1995**, *67*, 3377−3381.
(4) Levin, I. W.; Bhargava, R. *Annu. Rev. Phys. Chem.* **2005**, *56*, 429−474.
(5) Ogunleke, A.; Bobroff, V.; Chen, H.; Rowlette, J.; Delugin, M.; Recur, B.; Hwu, Y.; Petibois, C. *TrAC, Trends Anal. Chem.* **2017**, *89*, 190−196.
(6) Antonio, K. A.; Schultz, Z. D. *Anal. Chem.* **2014**, *86*, 30−46.
(7) Cucci, C.; Delaney, J. K.; Picollo, M. *Acc. Chem. Res.* **2016**, *49*, 2070−2079.
(8) Lopez-Lorente, A. I.; Mizaikoff, B. *TrAC, Trends Anal. Chem.* **2016**, *84*, 97−106.
(9) Ewing, A. V.; Kazarian, S. G. *Analyst* **2017**, *142*, 257−272.
(10) Blasiak, B.; Londergan, C. H.; Webb, L. J.; Cho, M. *Acc. Chem. Res.* **2017**, *50*, 968−976.
(11) Wei, L.; Chen, Z.; Shi, L.; Long, R.; Anzalone, A. V.; Zhang, L.; Hu, F.; Yuste, R.; Cornish, V. W.; Min, W. *Nature* **2017**, *544*, 465−470.
(12) Lane, L. A.; Qian, X.; Nie, S. *Chem. Rev.* **2015**, *115*, 10489−10529.
(13) Fabris, L. *Chemnanomat.* **2016**, *2*, 249−258.
(14) Anderson, M. *Appl. Phys. Lett.* **2000**, *76*, 3130−3132.
(15) Hayazawa, N.; Inouye, Y.; Sekkat, Z.; Kawata, S. *Opt. Commun.* **2000**, *183*, 333−336.
(16) Pettinger, B.; Picardi, G.; Schuster, R.; Ertl, G. *Electrochemistry-Tokyo* **2000**, *68*, 942−949.
(17) Stockle, R.; Suh, Y.; Deckert, V.; Zenobi, R. *Chem. Phys. Lett.* **2000**, *318*, 131−136.
(18) Zhang, Z.; Sheng, S.; Wang, R.; Sun, M. *Anal. Chem.* **2016**, *88*, 9328−9346.
(19) Verma, P. *Chem. Rev.* **2017**, *117*, 6447−6466.
(20) Shi, X.; Coca-Lopez, N.; Janik, J.; Hartschuh, A. *Chem. Rev.* **2017**, DOI: 10.1021/acs.chemrev.6b00640.
(21) Deckert-Gaudig, T.; Taguchi, A.; Kawata, S.; Deckert, V. *Chem. Soc. Rev.* **2017**, *46*, 4077−4110.
(22) Wang, X.; Huang, S. C.; Huang, T. X.; Su, H. S.; Zhong, J. H.; Zeng, Z. C.; Li, M. H.; Ren, B. *Chem. Soc. Rev.* **2017**, *46*, 4020−4041.
(23) Li, M.; Lv, R.; Huang, S.; Dai, Y.; Zeng, Z.; Wang, L.; Ren, B. *J. Raman Spectrosc.* **2016**, *47*, 808−812.
(24) Huh, T. W.; Han, G.; Ban, W. J.; Ahn, H. *Int. J. Precis. Eng. Manuf.* **2017**, *18*, 221−226.
(25) Martina, M.; Fleischer, M.; Burkhardt, C. J. *Microelectron. Eng.* **2017**, *171*, 31−36.
(26) Kharintsev, S.; Alekseev, A.; Loos, J. *Spectrochim. Acta, Part A* **2017**, *171*, 139−143.
(27) Lee, C.; Kim, S. T.; Jeong, B. G.; Yun, S. J.; Song, Y. J.; Lee, Y. H.; Park, D. J.; Jeong, M. S. *Sci. Rep.* **2017**, *7*, 40810.
(28) Leiterer, C.; Deckert-Gaudig, T.; Singh, P.; Wirth, J.; Deckert, V.; Fritzsche, W. *Electrophoresis* **2015**, *36*, 1142−1148.
(29) Kim, W.; Kim, N.; Lee, E.; Kim, D.; Hwan Kim, Z.; Won Park, J. *Analyst* **2016**, *141*, 5066−5070.
(30) Zito, G.; Rusciano, G.; Vecchione, A.; Pesce, G.; Di Girolamo, R.; Malafronte, A.; Sasso, A. *Sci. Rep.* **2016**, *6*, 31113.
(31) Yang, L. K.; Huang, T. X.; Zeng, Z. C.; Li, M. H.; Wang, X.; Yang, F. Z.; Ren, B. *Nanoscale* **2015**, *7*, 18225−18231.
(32) Ma, X.; Gruesser, M.; Schuster, R. *Appl. Phys. Lett.* **2015**, *106*, 241103.
(33) Bakhti, S.; Destouches, N.; Hubert, C.; Reynaud, S.; Vocanson, F.; Ondarcuhu, T.; Epicier, T. *Nanoscale* **2016**, *8*, 7496−7500.
(34) Taguchi, A.; Yu, J.; Verma, P.; Kawata, S. *Nanoscale* **2015**, *7*, 17424−17433.
(35) Maouli, I.; Taguchi, A.; Saito, Y.; Kawata, S.; Verma, P. *Appl. Phys. Express* **2015**, *8*, 032401.
(36) Vasconcelos, T. L.; Archanjo, B. S.; Fragneaud, B.; Oliveira, B. S.; Riikonen, J.; Li, C.; Ribeiro, D. S.; Rabelo, C.; Rodrigues, W. N.; Jorio, A.; Achete, C. A.; Cancado, L. G. *ACS Nano* **2015**, *9*, 6297−6304.
(37) Kitahama, Y.; Uemura, S.; Katayama, R.; Suzuki, T.; Itoh, T.; Ozaki, Y. *Appl. Phys. Lett.* **2017**, *110*, 233104.
(38) Opilik, L.; Dogan, U.; Szczerbinski, J.; Zenobi, R. *Appl. Phys. Lett.* **2015**, *107*, 091109.
(39) Kumar, N.; Spencer, S. J.; Imbraguglio, D.; Rossi, A. M.; Wain, A. J.; Weckhuysen, B. M.; Roy, D. *Phys. Chem. Chem. Phys.* **2016**, *18*, 13710−13716.
(40) Opilik, L.; Dogan, U.; Li, C.; Stephanidis, B.; Li, J.; Zenobi, R. *J. Phys. Chem. C* **2016**, *120*, 20828−20832.
(41) Deckert, V.; Deckert-Gaudig, T.; Diegel, M.; Goetz, I.; Langelueddecke, L.; Schneidewind, H.; Sharma, G.; Singh, P.; Singh, P.; Trautmann, S.; Zeisberger, M.; Zhang, Z. *Faraday Discuss.* **2015**, *177*, 9−20.
(42) Jiang, S.; Zhang, Y.; Zhang, R.; Hu, C.; Liao, M.; Luo, Y.; Yang, J.; Dong, Z.; Hou, J. G. *Nat. Nanotechnol.* **2015**, *10*, 865−869.
(43) Liao, M.; Jiang, S.; Hu, C.; Zhang, R.; Kuang, Y.; Zhu, J.; Zhang, Y.; Dong, Z. *Nano Lett.* **2016**, *16*, 4040−4046.
(44) Chiang, N.; Chen, X.; Goubert, G.; Chulhai, D. V.; Chen, X.; Pozzi, E. A.; Jiang, N.; Hersam, M. C.; Seideman, T.; Jensen, L.; Van Duyne, R. P. *Nano Lett.* **2016**, *16*, 7774−7778.
(45) Deckert-Gaudig, T.; Kurouski, D.; Hedegaard, M. A. B.; Singh, P.; Lednev, I. K.; Deckert, V. *Sci. Rep.* **2016**, *6*, 33575.
(46) Zhang, R.; Zhang, X.; Wang, H.; Zhang, Y.; Jiang, S.; Hu, C.; Zhang, Y.; Luo, Y.; Dong, Z. *Angew. Chem., Int. Ed.* **2017**, *56*, 5561−5564.
(47) Pozzi, E. K.; Goubert, G.; Chiang, N.; Jiang, N.; Chapman, C. T.; McAnally, M. O.; Henry, A.; Seideman, T.; Schatz, G. C.; Hersam, M. C.; Van Duyne, R. P. *Chem. Rev.* **2017**, *117*, 4961−4982.
(48) Meng, L.; Yang, Z.; Chen, J.; Sun, M. *Sci. Rep.* **2015**, *5*, 9240.
(49) Zhang, C.; Chen, B.; Li, Z. *J. Phys. Chem. C* **2015**, *119*, 11858−11871.
(50) Zhang, C.; Chen, B.; Li, Z. *Chin. Phys. B* **2016**, *25*, 095203.
(51) Trautmann, S.; Aizpurua, J.; Goetz, I.; Undisz, A.; Dellith, J.; Schneidewind, H.; Rettenmayr, M.; Deckert, V. *Nanoscale* **2017**, *9*, 391−401.
(52) Latorre, F.; Kupfer, S.; Bocklitz, T.; Kinzel, D.; Trautmann, S.; Graefe, S.; Deckert, V. *Nanoscale* **2016**, *8*, 10229−10239.
(53) Liu, P.; Chulhai, D. V.; Jensen, L. *ACS Nano* **2017**, *11*, 5094−5102.
(54) Dresselhaus, M. S.; Jorio, A.; Hofmann, M.; Dresselhaus, G.; Saito, R. *Nano Lett.* **2010**, *10*, 751−758.
(55) Beams, R.; Cançado, L. G.; Jorio, A.; Vamivakas, A. N.; Novotny, L. *Nanotechnology* **2015**, *26*, 175702.
(56) Vantasin, S.; Tanaka, Y.; Uemura, S.; Suzuki, T.; Kutsuma, Y.; Doujima, D.; Kaneko, T.; Ozaki, Y. *Phys. Chem. Chem. Phys.* **2015**, *17*, 28993−28999.
(57) Iwasaki, T.; Zelai, T.; Ye, S.; Tsuchiya, Y.; Chong, H. M.; Mizuta, H. *Carbon* **2017**, *111*, 67−73.
(58) Pashaee, F.; Sharifi, F.; Fanchini, G.; Lagugné-Labarthet, F. *Phys. Chem. Chem. Phys.* **2015**, *17*, 21315−21322.

DOI: 10.1021/acs.analchem.7b04151
Anal. Chem. 2018, 90, 440−458

(59) Su, W.; Kumar, N.; Dai, N.; Roy, D. *Chem. Commun. (Cambridge, U. K.)* **2016**, *52*, 8227−8230.
(60) Chaunchaiyakul, S.; Yano, T.; Khoklang, K.; Krukowski, P.; Akai-Kasaya, M.; Saito, A.; Kuwahara, Y. *Carbon* **2016**, *99*, 642−648.
(61) Hoffmann, G. G.; Bârsan, O. A.; Ven, L. G.; With, G. *J. Raman Spectrosc.* **2017**, *48*, 191−196.
(62) Sheremet, E.; Rodriguez, R. D.; Agapov, A. L.; Sokolov, A. P.; Hietschold, M.; Zahn, D. R. *Carbon* **2016**, *96*, 588−593.
(63) Wang, X.; Zhong, J.; Zhang, M.; Liu, Z.; Wu, D.; Ren, B. *Anal. Chem.* **2016**, *88*, 915−921.
(64) Opilik, L.; Payamyar, P.; Szczerbiński, J.; Schütz, A. P.; Servalli, M.; Hungerland, T.; Schlüter, A. D.; Zenobi, R. *ACS Nano* **2015**, *9*, 4252−4259.
(65) Shao, F.; Müller, V.; Zhang, Y.; Schlüter, A. D.; Zenobi, R. *Angew. Chem.* **2017**, *129*, 9489−9494.
(66) Su, W.; Kumar, N.; Mignuzzi, S.; Crain, J.; Roy, D. *Nanoscale* **2016**, *8*, 10564−10569.
(67) Park, K.; Khatib, O.; Kravtsov, V.; Clark, G.; Xu, X.; Raschke, M. B. *Nano Lett.* **2016**, *16*, 2621−2627.
(68) Zhang, Y.; Voronine, D. V.; Qiu, S.; Sinyukov, A. M.; Hamilton, M.; Liege, Z.; Sokolov, A. V.; Zhang, Z.; Scully, M. O. *Sci. Rep.* **2016**, *6*, 25788.
(69) Rodriguez, R. D.; Sheremet, E.; Deckert-Gaudig, T.; Chaneac, C.; Hietschold, M.; Deckert, V.; Zahn, D. R. *Nanoscale* **2015**, *7*, 9545−9551.
(70) Meyer, C.; Hühn, S.; Jungbauer, M.; Merten, S.; Damaschke, B.; Samwer, K.; Moshnyaga, V. *J. Raman Spectrosc.* **2017**, *48*, 46−52.
(71) Lucia, A.; Cacioppo, O. A.; Iulianella, E.; Latessa, L.; Moccia, G.; Passeri, D.; Rossi, M. *Appl. Phys. Lett.* **2017**, *110*, 103105.
(72) Lin, X.; Deckert-Gaudig, T.; Singh, P.; Siegmann, M.; Kupfer, S.; Zhang, Z.; Gräfe, S.; Deckert, V. arXiv preprint, *arXiv:1604.06598*, 2016.
(73) Pashaee, F.; Tabatabaei, M.; Caetano, F. A.; Ferguson, S. S.; Lagugné-Labarthet, F. *Analyst* **2016**, *141*, 3251−3258.
(74) Japaridze, A.; Vobornik, D.; Lipiec, E.; Cerreta, A.; Szczerbinski, J.; Zenobi, R.; Dietler, G. *Macromolecules* **2016**, *49*, 643−652.
(75) Lipiec, E.; Japaridze, A.; Szczerbiński, J.; Dietler, G.; Zenobi, R. *Small* **2016**, *12*, 4821−4829.
(76) Deckert-Gaudig, T.; Deckert, V. *Sci. Rep.* **2016**, *6*, 39622.
(77) Sereda, V.; Lednev, I. K. *Appl. Spectrosc.* **2017**, *71*, 118−128.
(78) Krasnoslobodtsev, A. V.; Deckert-Gaudig, T.; Zhang, Y.; Deckert, V.; Lyubchenko, Y. L. *Ultramicroscopy* **2016**, *165*, 26−33.
(79) VandenAkker, C. C.; Schleeger, M.; Bruinen, A. L.; Deckert-Gaudig, T.; Velikov, K. P.; Heeren, R. M. A.; Deckert, V.; Bonn, M.; Koenderink, G. H. *J. Phys. Chem. B* **2016**, *120*, 8809−8817.
(80) VandenAkker, C. C.; Deckert-Gaudig, T.; Schleeger, M.; Velikov, K. P.; Deckert, V.; Bonn, M.; Koenderink, G. H. *Small* **2015**, *11*, 4131−4139.
(81) Bonhommeau, S.; Talaga, D.; Hunel, J.; Cullin, C.; Lecomte, S. *Angew. Chem., Int. Ed.* **2017**, *56*, 1771−1774.
(82) Blum, C.; Schmid, T.; Opilik, L.; Metanis, N.; Weidmann, S.; Zenobi, R. *J. Phys. Chem. C* **2012**, *116*, 23061−23066.
(83) Davies, H. S.; Singh, P.; Deckert-Gaudig, T.; Deckert, V.; Rousseau, K.; Ridley, C. E.; Dowd, S. E.; Doig, A. J.; Pudney, P. D. A.; Thornton, D. J.; Blanch, E. W. *Anal. Chem.* **2016**, *88*, 11609−11615.
(84) Cowcher, D. P.; Deckert-Gaudig, T.; Brewster, V. L.; Ashton, L.; Deckert, V.; Goodacre, R. *Anal. Chem.* **2016**, *88*, 2105−2112.
(85) Carrier, S. L.; Kownacki, C. M.; Schultz, Z. D. *Chem. Commun. (Cambridge, U. K.)* **2011**, *47*, 2065−2067.
(86) Alexander, K. D.; Schultz, Z. D. *Anal. Chem.* **2012**, *84*, 7408−7414.
(87) Wang, H.; Schultz, Z. D. *Analyst* **2013**, *138*, 3150−3157.
(88) Wang, H.; Schultz, Z. D. *ChemPhysChem* **2014**, *15*, 3944−3949.
(89) Xiao, L.; Wang, H.; Schultz, Z. D. *Anal. Chem.* **2016**, *88*, 6547−6553.
(90) Xiao, L.; Bailey, K. A.; Wang, H.; Schultz, Z. D. *Anal. Chem.* **2017**, *89*, 9091−9099.
(91) Olschewski, K.; Kammer, E.; Stockel, S.; Bocklitz, T.; Deckert-Gaudig, T.; Zell, R.; Cialla-May, D.; Weber, K.; Deckert, V.; Popp, J. *Nanoscale* **2015**, *7*, 4545−4552.
(92) Hermelink, A.; Naumann, D.; Piesker, J.; Lasch, P.; Laue, M.; Hermann, P. *Analyst* **2017**, *142*, 1342−1349.
(93) Rusciano, G.; Zito, G.; Isticato, R.; Sirec, T.; Ricca, E.; Bailo, E.; Sasso, A. *ACS Nano* **2014**, *8*, 12300−12309.
(94) Kumar, N.; Drozdz, M. M.; Jiang, H.; Santos, D. M.; Vaux, D. J. *Chem. Commun. (Cambridge, U. K.)* **2017**, *53*, 2451−2454.
(95) Ashtikar, M.; Langelüddecke, L.; Fahr, A.; Deckert, V. *Biochim. Biophys. Acta, Gen. Subj.* **2017**, *1861*, 2630−2639.
(96) Schmid, T.; Yeo, B.; Leong, G.; Stadler, J.; Zenobi, R. *J. Raman Spectrosc.* **2009**, *40*, 1392−1399.
(97) Nakata, A.; Nomoto, T.; Toyota, T.; Fujinami, M. *Anal. Sci.* **2013**, *29*, 865−869.
(98) Pienpinijtham, P.; Vantasin, S.; Kitahama, Y.; Ekgasit, S.; Ozaki, Y. *J. Phys. Chem. C* **2016**, *120*, 14663−14668.
(99) Zeng, Z.; Huang, S.; Wu, D.; Meng, L.; Li, M.; Huang, T.; Zhong, J.; Wang, X.; Yang, Z.; Ren, B. *J. Am. Chem. Soc.* **2015**, *137*, 11928−11931.
(100) Kurouski, D.; Mattei, M.; Van Duyne, R. P. *Nano Lett.* **2015**, *15*, 7956−7962.
(101) Touzalin, T.; Dauphin, A. L.; Joiret, S.; Lucas, I. T.; Maisonhaute, E. *Phys. Chem. Chem. Phys.* **2016**, *18*, 15510−15513.
(102) Martin Sabanes, N.; Driessen, L. M. A.; Domke, K. F. *Anal. Chem.* **2016**, *88*, 7108−7114.
(103) Kumar, N.; Stephanidis, B.; Zenobi, R.; Wain, A. J.; Roy, D. *Nanoscale* **2015**, *7*, 7133−7137.
(104) Zhong, J.; Jin, X.; Meng, L.; Wang, X.; Su, H.; Yang, Z.; Williams, C. T.; Ren, B. *Nat. Nanotechnol.* **2017**, *12*, 132−136.
(105) Tallarida, N.; Rios, L.; Apkarian, V. A.; Lee, J. *Nano Lett.* **2015**, *15*, 6386−6394.
(106) Jiang, N.; Chiang, N.; Madison, L. R.; Pozzi, E. A.; Wasielewski, M. R.; Seideman, T.; Ratner, M. A.; Hersam, M. C.; Schatz, G. C.; Van Duyne, R. P. *Nano Lett.* **2016**, *16*, 3898−3904.
(107) El-Khoury, P. Z.; Gong, Y.; Abellan, P.; Arey, B. W.; Joly, A. G.; Hu, D.; Evans, J. E.; Browning, N. D.; Hess, W. P. *Nano Lett.* **2015**, *15*, 2385−2390.
(108) Bhattarai, A.; El-Khoury, P. Z. *Chem. Commun. (Cambridge, U. K.)* **2017**, *53*, 7310−7313.
(109) Tranca, D. E.; Stanciu, S. G.; Hristu, R.; Stoichita, C.; Tofail, S. A.; Stanciu, G. A. *Sci. Rep.* **2015**, *5*, 11876.
(110) Pollard, B.; Maia, F. C.; Raschke, M. B.; Freitas, R. O. *Nano Lett.* **2016**, *16*, 55−61.
(111) Shi, Z.; Bechtel, H. A.; Berweger, S.; Sun, Y.; Zeng, B.; Jin, C.; Chang, H.; Martin, M. C.; Raschke, M. B.; Wang, F. *ACS Photonics* **2015**, *2*, 790−796.
(112) Alfaro-Mozaz, F. J.; Alonso-Gonzalez, P.; Velez, S.; Dolado, I.; Autore, M.; Mastel, S.; Casanova, F.; Hueso, L. E.; Li, P.; Nikitin, A. Y.; Hillenbrand, R. *Nat. Commun.* **2017**, *8*, 15624.
(113) Mastel, S.; Govyadinov, A. A.; de Oliveira, T. V.; Amenabar, I.; Hillenbrand, R. *Appl. Phys. Lett.* **2015**, *106*, 023113.
(114) Atkin, J. M.; Berweger, S.; Jones, A. C.; Raschke, M. B. *Adv. Phys.* **2012**, *61*, 745−842.
(115) Centrone, A. *Annu. Rev. Anal. Chem.* **2015**, *8*, 101−126.
(116) Yoxall, E.; Schnell, M.; Mastel, S.; Hillenbrand, R. *Opt. Express* **2015**, *23*, 13358−13369.
(117) Wang, H.; Wang, L.; Xu, X. G. *Nat. Commun.* **2016**, *7*, 13212.
(118) Amenabar, I.; Poly, S.; Goikoetxea, M.; Nuansing, W.; Lasch, P.; Hillenbrand, R. *Nat. Commun.* **2017**, *8*, 14402.
(119) O'Callahan, B. T.; Lewis, W. E.; Möbius, S.; Stanley, J. C.; Muller, E. A.; Raschke, M. B. *Opt. Express* **2015**, *23*, 32063−32074.
(120) Lahneman, D.; Huffman, T.; Xu, P.; Wang, S.; Grogan, T.; Qazilbash, M. *Opt. Express* **2017**, *25*, 20421−20430.
(121) Ellis, G. J.; Martin, M. C. *Eur. Polym. J.* **2016**, *81*, 505−531.
(122) Patoka, P.; Ulrich, G.; Nguyen, A. E.; Bartels, L.; Dowben, P. A.; Turkowski, V.; Rahman, T. S.; Hermann, P.; Kästner, B.; Hoehl, A. *Opt. Express* **2016**, *24*, 1154−1164.

DOI: 10.1021/acs.analchem.7b04151
Anal. Chem. 2018, 90, 440−458

(123) Hermann, P.; Kästner, B.; Hoehl, A.; Kashcheyevs, V.; Patoka, P.; Ulrich, G.; Feikes, J.; Ries, M.; Tydecks, T.; Beckhoff, B. *Opt. Express* **2017**, *25*, 16574−16588.
(124) Kehr, S. C.; Döring, J.; Gensch, M.; Helm, M.; Eng, L. M. *Synchrotron Radiat.News.* **2017**, *30*, 31−35.
(125) Lin, K.; Komiyama, S.; Kajihara, Y. *Opt. Lett.* **2016**, *41*, 484−487.
(126) Lin, K.; Komiyama, S.; Kim, S.; Kawamura, K.; Kajihara, Y. *Rev. Sci. Instrum.* **2017**, *88*, 013706.
(127) Wagner, M.; Andreev, G.; Carneiro, K.; Habelitz, S.; Mueller, T. *Microsc. Microanal.* **2015**, *21*, 1873.
(128) Pollard, B.; Raschke, M. B. *Beilstein J. Nanotechnol.* **2016**, *7*, 605.
(129) Xu, X. G.; Gilburd, L.; Bando, Y.; Golberg, D.; Walker, G. C. *J. Phys. Chem. C* **2016**, *120*, 1945−1951.
(130) Eisele, M.; Cocker, T. L.; Huber, M. A.; Plankl, M.; Viti, L.; Ercolani, D.; Sorba, L.; Vitiello, M. S.; Huber, R. *Nat. Photonics* **2014**, *8*, 841−845.
(131) Wagner, M.; McLeod, A. S.; Maddox, S. J.; Fei, Z.; Liu, M.; Averitt, R. D.; Fogler, M. M.; Bank, S. R.; Keilmann, F.; Basov, D. *Nano Lett.* **2014**, *14*, 4529−4534.
(132) Dönges, S. A.; Khatib, O.; O'Callahan, B. T.; Atkin, J. M.; Park, J. H.; Cobden, D.; Raschke, M. B. *Nano Lett.* **2016**, *16*, 3029−3035.
(133) Huber, M. A.; Plankl, M.; Eisele, M.; Marvel, R.; Sandner, F.; Korn, T.; Schüller, C.; Haglund, R., Jr; Huber, R.; Cocker, T. L. *Nano Lett.* **2016**, *16*, 1421−1427.
(134) Dai, S.; Ma, Q.; Liu, M.; Andersen, T.; Fei, Z.; Goldflam, M.; Wagner, M.; Watanabe, K.; Taniguchi, T.; Thiemens, M. *Nat. Nanotechnol.* **2015**, *10*, 682−686.
(135) Barcelos, I. D.; Cadore, A. R.; Campos, L. C.; Malachias, A.; Watanabe, K.; Taniguchi, T.; Maia, F. C.; Freitas, R.; Deneke, C. *Nanoscale* **2015**, *7*, 11620−11625.
(136) Kang, J.; Wang, S.; Shi, Z.; Zhao, W.; Yablonovitch, E.; Wang, F. *Nano Lett.* **2017**, *17*, 1768−1774.
(137) Kim, K. S.; Trajanoski, D.; Ho, K.; Gilburd, L.; Maiti, A.; van der Velden, L.; de Beer, S.; Walker, G. C. *J. Phys. Chem. Lett.* **2017**, *8*, 2902−2908.
(138) Bezares, F. J.; De Sanctis, A.; Saavedra, J. R.; Woessner, A.; Alonso-González, P.; Amenabar, I.; Chen, J.; Bointon, T.; Dai, S.; Fogler, M. M. *Nano Lett.* **2017**, *17*, 5908.
(139) Levratovsky, Y.; Gross, E. *Faraday Discuss.* **2016**, *188*, 345−353.
(140) Johnson, C. M.; Böhmler, M. *Corros. Sci.* **2016**, *108*, 60−65.
(141) Ayache, M.; Lux, S. F.; Kostecki, R. *J. Phys. Chem. Lett.* **2015**, *6*, 1126−1129.
(142) Khanikaev, A. B.; Arju, N.; Fan, Z.; Purtseladze, D.; Lu, F.; Lee, J.; Sarriugarte, P.; Schnell, M.; Hillenbrand, R.; Belkin, M. A.; Shvets, G. *Nat. Commun.* **2016**, *7*, 12045.
(143) Muller, E. A.; Pollard, B.; Bechtel, H. A.; van Blerkom, P.; Raschke, M. B. *Sci.Adv.* **2016**, *2*, e1601006.
(144) Liu, M.; Sternbach, A. J.; Wagner, M.; Slusar, T. V.; Kong, T.; Bud'ko, S. L.; Kittiwatanakul, S.; Qazilbash, M.; McLeod, A.; Fei, Z. *Phys. Rev. B* **2015**, *91*, 245155.
(145) Atkin, J. M.; Sass, P. M.; Teichen, P. E.; Eaves, J. D.; Raschke, M. B. *J. Phys. Chem. Lett.* **2015**, *6*, 4616−4621.
(146) Amrania, H.; Drummond, L.; Coombes, R.; Shousha, S.; Woodley-Barker, L.; Weir, K.; Hart, W.; Carter, I.; Phillips, C. *Faraday Discuss.* **2016**, *187*, 539−553.
(147) Qin, N.; Zhang, S.; Jiang, J.; Corder, S. G.; Qian, Z.; Zhou, Z.; Lee, W.; Liu, K.; Wang, X.; Li, X.; Shi, Z.; Mao, Y.; Bechtel, H. A.; Martin, M. C.; Xia, X.; Marelli, B.; Kaplan, D. L.; Omenetto, F. G.; Liu, M.; Tao, T. H. *Nat. Commun.* **2016**, *7*, 13079.
(148) Carneiro, K. M.; Zhai, H.; Zhu, L.; Horst, J. A.; Sitlin, M.; Nguyen, M.; Wagner, M.; Simpliciano, C.; Milder, M.; Chen, C. *Sci. Rep.* **2016**, *6*, 23105.
(149) Wiens, R.; Findlay, C. R.; Baldwin, S. G.; Kreplak, L.; Lee, J. M.; Veres, S. P.; Gough, K. M. *Faraday Discuss.* **2016**, *187*, 555−573.
(150) Khatib, O.; Wood, J. D.; McLeod, A. S.; Goldflam, M. D.; Wagner, M.; Damhorst, G. L.; Koepke, J. C.; Doidge, G. P.; Rangarajan, A.; Bashir, R. *ACS Nano* **2015**, *9*, 7968−7975.
(151) Dazzi, A.; Prazeres, R.; Glotin, F.; Ortega, J. *Opt. Lett.* **2005**, *30*, 2388−2390.
(152) Dazzi, A.; Prater, C. B. *Chem. Rev.* **2016**, *117*, 5146−5173.
(153) Lu, F.; Jin, M.; Belkin, M. A. *Nat. Photonics* **2014**, *8*, 307−312.
(154) Dazzi, A.; Saunier, J.; Kjoller, K.; Yagoubi, N. *Int. J. Pharm.* **2015**, *484*, 109−114.
(155) Ramer, G.; Balbekova, A.; Schwaighofer, A.; Lendl, B. *Anal. Chem.* **2015**, *87*, 4415−4420.
(156) Jin, M.; Lu, F.; Belkin, M. A. *Light: Sci. Appl.* **2017**, *6*, e17096.
(157) Baldassarre, L.; Giliberti, V.; Rosa, A.; Ortolani, M.; Bonamore, A.; Baiocco, P.; Kjoller, K.; Calvani, P.; Nucara, A. *Nanotechnology* **2016**, *27*, 075101.
(158) Giliberti, V.; Badioli, M.; Baldassarre, L.; Nucara, A.; Calvani, P.; Ritter, E.; Puskar, L.; Hegemann, P.; Schade, U.; Ortolani, M. *41st International Conference on Infrared, Millimeter, and Terahertz Waves (IRMMW-THZ)*, Copenhagen, Denmark, September 25−30, 2016.
(159) Giliberti, V.; Badioli, M.; Baldassarre, L.; Nucara, A.; Calvani, P.; Ritter, E.; Puskar, L.; Hegemann, P.; Schade, U.; Ortolani, M. *Proc. SPIE* **2017**, *10111*, 101110D.
(160) Ramer, G.; Reisenbauer, F.; Steindl, B.; Tomischko, W.; Lendl, B. *Appl. Spectrosc.* **2017**, *71*, 2013−2020.
(161) Donaldson, P. M.; Kelley, C. S.; Frogley, M. D.; Filik, J.; Wehbe, K.; Cinque, G. *Opt. Express* **2016**, *24*, 1852−1864.
(162) Katzenmeyer, A. M.; Holland, G.; Kjoller, K.; Centrone, A. *Anal. Chem.* **2015**, *87*, 3154−3159.
(163) Lo, M. K.; Dazzi, A.; Marcott, C. A.; Dillon, E.; Hu, Q.; Kjoller, K.; Prater, C. B.; King, S. W. *ECS J. Solid State Sci. Technol.* **2016**, *5*, P3018−P3024.
(164) Vitry, P.; Rebois, R.; Bourillot, E.; Deniset-Besseau, A.; Virolle, M.; Lesniewska, E.; Dazzi, A. *Nano Res.* **2016**, *9*, 1674−1681.
(165) Latour, G.; Robinet, L.; Dazzi, A.; Portier, F.; Deniset-Besseau, A.; Schanne-Klein, M. C. *Sci. Rep.* **2016**, *6*, 26344.
(166) Katzenmeyer, A. M.; Holland, G.; Chae, J.; Band, A.; Kjoller, K.; Centrone, A. *Nanoscale* **2015**, *7*, 17637−17641.
(167) Wang, L.; Wang, H.; Wagner, M.; Yan, Y.; Jakob, D. S.; Xu, X. G. *Sci.Adv.* **2017**, *3*, e1700255.
(168) Brown, P. S.; Bhushan, B. *Sci. Rep.* **2016**, *6*, 21048.
(169) Tang, F.; Bao, P.; Su, Z. *Anal. Chem.* **2016**, *88*, 4926−4930.
(170) Kelchtermans, M.; Lo, M.; Dillon, E.; Kjoller, K.; Marcott, C. *Vib. Spectrosc.* **2016**, *82*, 10−15.
(171) Sang, J.; Sato, R.; Aisawa, S.; Hirahara, H.; Mori, K. *Appl. Surf. Sci.* **2017**, *412*, 121−130.
(172) Urbanek, O.; Sajkiewicz, P.; Pierini, F.; Czerkies, M.; Kołbuk, D. *Biomed.Mater.* **2017**, *12*, 015020.
(173) Tang, J.; Liu, Y.; Zhu, B.; Su, Y.; Zhu, X. *Appl. Surf. Sci.* **2017**, *393*, 299−308.
(174) Cui, Z.; Coletta, C.; Rebois, R.; Baiz, S.; Gervais, M.; Goubard, F.; Aubert, P.; Dazzi, A.; Remita, S. *Radiat. Phys. Chem.* **2016**, *119*, 157−166.
(175) Coletta, C.; Cui, Z.; Dazzi, A.; Guigner, J.; Néron, S.; Marignier, J.; Remita, S. *Radiat. Phys. Chem.* **2016**, *126*, 21−31.
(176) Ghosh, S.; Kouamé, N. A.; Ramos, L.; Remita, S.; Dazzi, A.; Deniset-Besseau, A.; Beaunier, P.; Goubard, F.; Aubert, P.; Remita, H. *Nat. Mater.* **2015**, *14*, 505.
(177) Ghosh, S.; Ramos, L.; Remita, S.; Dazzi, A.; Deniset-Besseau, A.; Beaunier, P.; Goubard, F.; Aubert, P.; Remita, H. *New J. Chem.* **2015**, *39*, 8311−8320.
(178) Gong, L.; Chase, D. B.; Noda, I.; Liu, J.; Martin, D. C.; Ni, C.; Rabolt, J. F. *Macromolecules* **2015**, *48*, 6197−6205.
(179) Gong, L.; Chase, D. B.; Noda, I.; Marcott, C. A.; Liu, J.; Martin, D. C.; Ni, C.; Rabolt, J. F. *Macromolecules* **2017**, *50*, 5510−5517.
(180) Purohit, H. S.; Taylor, L. S. *Mol. Pharmaceutics* **2015**, *12*, 4542−4553.
(181) Li, N.; Taylor, L. S. *Mol. Pharmaceutics* **2016**, *13*, 1123−1136.

DOI: 10.1021/acs.analchem.7b04151
Anal. Chem. 2018, 90, 440−458

(182) Morsch, S.; Lyon, S.; Smith, S. D.; Gibbon, S. R. *Prog. Org. Coat.* **2015**, *86*, 173−180.
(183) Morsch, S.; Lyon, S.; Greensmith, P.; Smith, S. D.; Gibbon, S. R. *Faraday Discuss.* **2015**, *180*, 527−542.
(184) Morsch, S.; Lyon, S.; Gibbon, S. *Prog. Org. Coat.* **2017**, *102*, 37−43.
(185) Morsch, S.; Liu, Y.; Lyon, S. B.; Gibbon, S. R. *ACS Appl. Mater. Interfaces* **2016**, *8*, 959−966.
(186) Morsch, S.; Liu, Y.; Greensmith, P.; Lyon, S. B.; Gibbon, S. R. *Polymer* **2017**, *108*, 146−153.
(187) Morsch, S.; van Driel, B. A.; van den Berg, K. J.; Dik, J. *ACS Appl. Mater. Interfaces* **2017**, *9*, 10169−10179.
(188) Kennedy, E.; Al-Majmaie, R.; Al-Rubeai, M.; Zerulla, D.; Rice, J. H. *J.Biophotonics.* **2015**, *8*, 133−141.
(189) Quaroni, L.; Pogoda, K.; Zuber, J.; Kwiatek, W. arXiv preprint, *arXiv:1704.01395*, 2017.
(190) Giliberti, V.; Baldassarre, L.; Rosa, A.; de Turris, V.; Ortolani, M.; Calvani, P.; Nucara, A. *Nanoscale* **2016**, *8*, 17560−17567.
(191) Gruszecki, W.; Kulik, A.; Janik, E.; Bednarska, J.; Luchowski, R.; Grudzinski, W.; Dietler, G. *Nanoscale* **2015**, *7*, 14659−14662.
(192) Rebois, R.; Onidas, D.; Marcott, C.; Noda, I.; Dazzi, A. *Anal. Bioanal. Chem.* **2017**, *409*, 2353−2361.
(193) Wang, X.; Deng, Y.; Li, Y.; Kjoller, K.; Roy, A.; Wang, S. *RSC Adv.* **2016**, *6*, 76318−76324.
(194) Barlow, D. E.; Biffinger, J. C.; Cockrell-Zugell, A. L.; Lo, M.; Kjoller, K.; Cook, D.; Lee, W. K.; Pehrsson, P. E.; Crookes-Goodson, W. J.; Hung, C. *Analyst* **2016**, *141*, 4848−4854.
(195) Khanal, D.; Kondyurin, A.; Hau, H.; Knowles, J. C.; Levinson, O.; Ramzan, I.; Fu, D.; Marcott, C.; Chrzanowski, W. *Anal. Chem.* **2016**, *88*, 7530−7538.
(196) Paluszkiewicz, C.; Piergies, N.; Chaniecki, P.; Rękas, M.; Miszczyk, J.; Kwiatek, W. *J. Pharm. Biomed. Anal.* **2017**, *139*, 125−132.
(197) Ruggeri, F. S.; Byrne, C.; Khemtemourian, L.; Ducouret, G.; Dietler, G.; Jacquot, Y. *J. Pept. Sci.* **2015**, *21*, 95−104.
(198) Ruggeri, F.; Longo, G.; Faggiano, S.; Lipiec, E.; Pastore, A.; Dietler, G. *Nat. Commun.* **2015**, *6*, 7831.
(199) Ruggeri, F. S.; Vieweg, S.; Cendrowska, U.; Longo, G.; Chiki, A.; Lashuel, H. A.; Dietler, G. *Sci. Rep.* **2016**, *6*, 31155.
(200) Volpatti, L. R.; Shimanovich, U.; Ruggeri, F. S.; Bolisetty, S.; Müller, T.; Mason, T. O.; Michaels, T. C.; Mezzenga, R.; Dietler, G.; Knowles, T. P. *J. Mater. Chem. B* **2016**, *4*, 7989−7999.
(201) Galante, D.; Ruggeri, F. S.; Dietler, G.; Pellistri, F.; Gatta, E.; Corsaro, A.; Florio, T.; Perico, A.; D'Arrigo, C. *Int. J. Biochem. Cell Biol.* **2016**, *79*, 261−270.
(202) Hu, Q.; Kjoller, K.; Myers, A.; Singh, K. J.; King, S. W. *Vib. Spectrosc.* **2016**, *86*, 223−232.
(203) Chae, J.; Dong, Q.; Huang, J.; Centrone, A. *Nano Lett.* **2015**, *15*, 8114−8121.
(204) Yuan, Y.; Chae, J.; Shao, Y.; Wang, Q.; Xiao, Z.; Centrone, A.; Huang, J. *Adv.Energy Mater.* **2015**, *5*, 1500615.
(205) Yoon, Y.; Chae, J.; Katzenmeyer, A. M.; Yoon, H. P.; Schumacher, J.; An, S.; Centrone, A.; Zhitenev, N. *Nanoscale* **2017**, *9*, 7771−7780.
(206) Strelcov, E.; Dong, Q.; Li, T.; Chae, J.; Shao, Y.; Deng, Y.; Gruverman, A.; Huang, J.; Centrone, A. *Sci.Adv.* **2017**, *3*, e1602165.
(207) Aksyuk, V.; Lahiri, B.; Holland, G.; Centrone, A. *Nanoscale* **2015**, *7*, 3634−3644.
(208) Chae, J.; Lahiri, B.; Kohoutek, J.; Holland, G.; Lezec, H.; Centrone, A. *Opt. Express* **2015**, *23*, 25912−25922.
(209) Chae, J.; Lahiri, B.; Centrone, A. *ACS Photonics* **2016**, *3*, 87−95.
(210) Jahng, J.; Ladani, F. T.; Khan, R. M.; Potma, E. O. *Proc. SPIE* **2016**, *9764*, 97641J.
(211) Ladani, F. T.; Potma, E. O. *Phys. Rev. B: Condens. Matter Mater. Phys.* **2017**, *95*, 205440.
(212) Jahng, J.; Fishman, D. A.; Park, S.; Nowak, D. B.; Morrison, W. A.; Wickramasinghe, H. K.; Potma, E. O. *Acc. Chem. Res.* **2015**, *48*, 2671−2679.
(213) Jahng, J.; Kim, B.; Lee, E. S.; Potma, E. O. *Phys. Rev. B: Condens. Matter Mater. Phys.* **2016**, *94*, 195407.
(214) Murdick, R. A.; Morrison, W.; Nowak, D.; Albrecht, T. R.; Jahng, J.; Park, S. *Jpn. J. Appl. Phys.* **2017**, *56*, 08LA04.
(215) Yamanishi, J.; Naitoh, Y.; Li, Y.; Sugawara, Y. *Appl. Phys. Lett.* **2017**, *110*, 123102.
(216) Jahng, J.; Ladani, F. T.; Khan, R. M.; Li, X.; Lee, E. S.; Potma, E. O. *Opt. Lett.* **2015**, *40*, 5058−5061.
(217) Ambrosio, A.; Devlin, R. C.; Capasso, F.; Wilson, W. L. *ACS Photonics* **2017**, *4*, 846−851.
(218) Huang, F.; Tamma, V. A.; Mardy, Z.; Burdett, J.; Wickramasinghe, H. K. *Sci. Rep.* **2015**, *5*, 10610.
(219) Tumkur, T. U.; Yang, X.; Cerjan, B.; Halas, N. J.; Nordlander, P.; Thomann, I. *Nano Lett.* **2016**, *16*, 7942−7949.
(220) Nowak, D.; Morrison, W.; Wickramasinghe, H. K.; Jahng, J.; Potma, E.; Wan, L.; Ruiz, R.; Albrecht, T. R.; Schmidt, K.; Frommer, J. *Sci. Adv.* **2016**, *2*, e1501571.
(221) Jacobs, I. E.; Aasen, E. W.; Nowak, D.; Li, J.; Morrison, W.; Roehling, J. D.; Augustine, M. P.; Moulé, A. J. *Adv. Mater.* **2017**, *29*, 1603221.
(222) Jahng, J.; Brocious, J.; Fishman, D. A.; Yampolsky, S.; Nowak, D.; Huang, F.; Apkarian, V. A.; Wickramasinghe, H. K.; Potma, E. O. *Appl. Phys. Lett.* **2015**, *106*, 083113.
(223) Tamma, V. A.; Huang, F.; Nowak, D.; Kumar Wickramasinghe, H. *Appl. Phys. Lett.* **2016**, *108*, 233107.
(224) Tamma, V. A.; Beecher, L. M.; Shumaker-Parry, J. S.; Wickramasinghe, H. K. arXiv preprint, *arXiv:1707.04986*, 2017.
(225) Kim, B.; Jahng, J.; Khan, R. M.; Park, S.; Potma, E. O. *Phys. Rev. B: Condens. Matter Mater. Phys.* **2017**, *95*, 075440.

DOI: 10.1021/acs.analchem.7b04151
Anal. Chem. 2018, 90, 440−458